Mechanisms of mitochondrial reactive oxygen species action in bone mesenchymal cells

Md Mohsin Ali[1], Intawat Nookaew[2,4], Ana Resende-Coelho[1], Adriana Marques-Carvalho[1], Aaron Warren[1], Qiang Fu[4], Ha-Neui Kim[1,4], Charles A O'Brien[1,3,4], Maria Almeida[1,3,4,5*]

[1]Division of Endocrinology and Metabolism, University of Arkansas for Medical Sciences, Little Rock, AR, USA

[2]Department of Biomedical Informatics; University of Arkansas for Medical Sciences, Little Rock, AR, USA

[3]Department of Orthopedic Surgery; University of Arkansas for Medical Sciences, Little Rock, AR, USA

[4]Center for Musculoskeletal Disease Research; University of Arkansas for Medical Sciences, Little Rock, AR, USA

[5]Lead contact

*Correspondence: Maria Almeida, Ph.D., 4301 W Markham Street, #587, Little Rock, Arkansas 72205, USA; Tel.: +1-501-686-7856; Fax +1-501-686-8148; Email: schullermaria@uams.edu

Summary

Mitochondrial (mt)ROS, insufficient NAD^+, and cellular senescence all contribute to the decrease in bone formation with aging. ROS can cause senescence and decrease NAD^+, but it remains unknown whether these mechanisms mediate the effects of ROS *in vivo*. Here, we generated mice lacking the mitochondrial antioxidant enzyme Sod2 in osteoblast lineage cells targeted by Osx1-Cre and showed that $Sod2^{\Delta Osx1}$ mice had low bone mass. Osteoblastic cells from these mice had impaired mitochondrial respiration and attenuated NAD^+ levels. Administration of an NAD^+ precursor improved mitochondrial function *in vitro* but failed to rescue the low bone mass of $Sod2^{\Delta Osx1}$ mice. Single-cell RNA-sequencing of bone mesenchymal cells indicated that ROS had no significant effects on markers of senescence but disrupted parathyroid hormone signaling, iron metabolism, and proteostasis. Our data supports the rationale that treatment combinations aimed at decreasing mtROS and senescent cells and increasing NAD^+ should confer additive effects in delaying age-associated osteoporosis.

Keywords

Skeletal aging; single-cell RNA sequencing; cellular senescence; mitochondrial dysfunction; NAD^+; nicotinamide riboside; proteostasis.

Introduction

Aging is a major cause of osteoporosis and increased fracture risk [1-5]. Age-related bone loss is primarily due to a decline in bone formation caused by a reduced number of osteoblasts — the cells responsible for the secretion of bone matrix [6]. Osteoblasts are short-lived cells that originate from mesenchymal precursors. We have previously shown that ROS increases in bone with aging and that suppression of mitochondrial ROS in all cells of the mesenchymal lineage, including stromal cells, osteoblasts precursors, osteoblasts, and osteocytes, attenuates age-associated bone loss [7]. In line with the damaging role of ROS in bone during aging, deletion of the antioxidant enzyme *Sod2* in cells of the osteoblast lineage in mice is sufficient to reduce bone formation and decrease bone mass in young adult mice [8,9].

The majority of cellular ROS are generated in the mitochondria during oxidative phosphorylation due to the leakage of electrons passing through the electron transport chain [10,11]. Electrons react with molecular oxygen to generate superoxide radicals (O2•–) which are rapidly converted to hydrogen peroxide (H_2O_2) by Cu/Zn-superoxide dismutase (Cu/ZnSOD or SOD1) and manganese-dependent superoxide dismutase (MnSOD or SOD2) [11,12]. One of the known roles for $O_2^{\bullet-}$ is the disruption of the Fe-S clusters in aconitase, a critical tricarboxylic acid (TCA) cycle enzyme [13,14]. Excessive ROS can also decrease the NAD^+/NADH redox balance, which is essential to cellular metabolism. Indeed, NADH is the major electron donor to complex I. NAD^+ is reduced back to NADH during multiple metabolic reactions but is also utilized by many NAD-dependent enzymes, including the poly (ADP-ribose) polymerases (PARPs) and sirtuin family of proteins [15]. We have shown previously that NAD^+ decreases with aging in osteoblastic cells and administration of NAD^+ precursors to mice attenuates the decrease in bone mass with aging [16].

Excessive ROS can also cause cellular senescence, and an increase in osteoblastic cell senescence contributes to the deficient bone formation and loss of bone mass with aging [17,18]. Senescent cells exhibit cell cycle arrest due to the upregulation of p16 (*Cdkn2a*) or p21 (*Cdkn1a*) [19,20]. Other changes in senescent cells include high senescence-associated β-galactosidase (SA-β-gal) activity, dysfunctional mitochondria, and secretion of an array of pro-inflammatory cytokines, chemokines, and proteases, known collectively as the senescence-associated secretory phenotype (SASP) [21-25]. SASP factors can either reinforce growth arrest in an autocrine manner or cause senescence in surrounding cells in a paracrine manner [26-28].

While an increase in ROS is a well-established cause of skeletal aging, the mechanisms that mediate the deleterious effects of ROS on bone formation remain unclear. It is also unknown whether excessive ROS in osteoblastic cells is causally related to other mechanisms of aging, such as senescence and decreased NAD^+. Understanding possible relationships between different mechanisms might contribute to the development of optimal treatment combinations to combat the loss of bone mass with aging.

Herein, we examined whether excessive levels of mtROS, such as that caused by *Sod2* deletion, are sufficient to cause other age-associated dysfunctions, such as cellular senescence and NAD^+ deficiency, and whether these effects could mediate the loss of bone mass due to mtROS. We also used the unbiased approach of single-cell RNA-sequencing (scRNA-seq) to identify potential mechanisms via which excessive mtROS affects mesenchymal bone cells.

Results

Deletion of *Sod2* in osteoblast lineage cells decreases bone mass

To investigate the effect of mtROS in cells of the osteoblast lineage, we generated mice in which cells targeted by an Osx1-Cre transgene were deficient in superoxide dismutase 2 (*Sod2*), referred to as Sod2$^{\Delta Osx1}$ mice, by crossing Osx1-Cre [29] with Sod2 floxed mice [30] (**Figure S1A; STAR Methods**). Osx1-Cre littermates were used as controls. Bone marrow stromal cell (BMSC) cultures of Sod2$^{\Delta Osx1}$ mice exhibited a decrease in *Sod2* mRNA levels, confirming effective deletion of the gene in the osteoblast lineage (**Figure 1A**). Three-month-old female Sod2$^{\Delta Osx1}$ mice had lower bone mineral density (BMD) both at the lumbar spine and femur, as determined by dual-energy X-ray absorptiometry (**Figure 1B; STAR Methods**). Likewise, male Sod2$^{\Delta Osx1}$ mice had reduced BMD at both sites (**Figure 1B**). Examination of bone microarchitecture by micro-computed tomography (µCT) analysis revealed that cortical thickness, measured at the femur midshaft, was lower in Sod2$^{\Delta Osx1}$ mice (**Figure 1C; STAR Methods**). Trabecular bone volume at the fifth lumbar vertebra (L5) was also lower in Sod2$^{\Delta Osx1}$ mice (**Figure 1D**). The lower bone volume was due to a decrease in trabecular number and was associated with an increase in trabecular separation. Trabecular thickness was not affected by *Sod2* deletion (**Figure S1B**). These results demonstrate that deletion of Sod2 in the osteoblast lineage is sufficient to decrease bone mass in young adult mice and confirm previous studies in which the gene was deleted with Dmp1-Cre and Runx2-Cre [8,9].

The mRNA levels of osteoblastic marker genes such as *Alpl*, *Bglap*, *Col1a1*, and *Sp7* were decreased in BMSCs derived from Sod2$^{\Delta Osx1}$ mice following 7 days of osteogenic differentiation (**Figure 1E; STAR Methods**). BrdU incorporation was also

reduced in these cells (**Figure 1F**). In line with these results, Alizarin Red S staining of the calcified matrix was substantially lower in cells with *Sod2* deletion (**Figure 1G**). These findings suggest that a decrease in osteoblast number contributes to the low bone mass caused by *Sod2* deletion, as shown by others using similar mouse models [8,9].

Deletion of *Sod2* causes mitochondrial dysfunction mimicking the effects of aging in BMSCs

We next examined the effects of *Sod2* deletion on mitochondrial biology. As anticipated, mtROS levels were elevated in BMSCS from $Sod2^{\Delta Osx1}$ mice compared to the control group, indicated by MitoSOX measurements (**Figure 2A**). Additionally, mitochondrial membrane potential ($\Delta\Psi m$), crucial for mitochondrial function, was decreased with *Sod2* deletion (**Figure 2B**). To evaluate mitochondrial respiration, we measured the oxygen consumption rate (OCR) in BMSCs. Both basal and maximal respiration were lower in cells from $Sod2^{\Delta Osx1}$ mice (**Figure 2C; STAR Methods**). Similar effects on mitochondria were seen in BMSCs cultured from old versus young wild-type mice. Specifically, cell cultures from 24-month-old C57BL/6 mice had higher mtROS, reduced $\Delta\Psi m$, and lower basal and maximal respiration when compared to cells from 6-month-old mice of the same strain (**Figure 2D and 2F**). These results support the idea that deletion of *Sod2* causes a dysfunction in mitochondria similar to that seen in old mice.

NR treatment increases NAD^+ and mitochondrial respiration in osteoblastic cells in culture

Elevated mtROS can decrease the levels of NAD^+ by impairing respiratory complex I and the oxidation of NADH to NAD^+ and by stimulating DNA repair enzymes that consume NAD^+ [31,32]. Cellular NAD^+ levels can be replenished by treatment with the NAD^+ precursor nicotinamide riboside (NR). We found that cultured *Sod2*-deficient BMSCs had lower NAD^+ than control cells (**Figure 3A**). Addition of NR to the cultures modestly increased NAD^+ in control cells and restored the basal levels of NAD^+ in cells from $Sod2^{\Delta Osx1}$ mice. We also assessed mitochondrial function by measuring OCR following 16 hours of NR treatment (**Figure 3B**). NR increased basal respiration in cells from $Sod2^{\Delta Osx1}$ mice. An increase in maximal respiration was seen in cells from both genotypes but was more robust in cells from $Sod2^{\Delta Osx1}$ mice **(Figure 3C**). These results demonstrated that NR supplementation attenuates the damaging effects of *Sod2* deletion in cells of the osteoblastic lineage and suggested that it might alleviate the negative effect on the skeleton.

NR supplementation does not rescue the low bone mass in $Sod2^{\Delta Osx1}$ mice

We next administered NR in the drinking water to 8-month-old control and $Sod2^{\Delta Osx1}$ mice for 4 months to evaluate its effects on bone mass (**Figure 3D**). We found that NAD^+ levels were increased in the fat tissue of NR-treated mice of both genotypes (**Figure 3F**). Nevertheless, this intervention did not alter BMD in the lumbar spine or femur, as both regions exhibited no significant changes compared to untreated

controls (**Figure 3E**). µCT analysis revealed that NR treatment did not alter bone volume fraction (BV/TV), trabecular separation, trabecular thickness, or trabecular number in lumbar vertebrae of Sod2$^{\Delta Osx1}$ or control mice (**Figure 3G and Figure S2A**). Cortical thickness**,** cortical area, and the ratio of cortical area to total cross-sectional area inside the periosteal envelope in the femur were also not affected by NR supplementation (**Figure 3H and Figure S2B**). Thus, while NR reduced signs of mitochondrial damage in osteoblast lineage cells, this was not sufficient to counteract the negative effects of Sod2 deletion.

scRNAseq reveals that *Sod2* deletion greatly changes the transcriptome of osteoblasts and adipo-CAR

To examine the transcriptional changes induced by elevated ROS in osteoblast lineage cells, we harvested endosteal cells from 4-month-old Sod2$^{\Delta Osx1}$ and littermate control mice. The endosteal cells were isolated from tibias and femurs after removing the periosteum, epiphyses, and bone marrow, followed by sequential incubations with collagenase and EDTA, as previously described [33] (**Figure 4A; STAR Methods**). A total of 15,224 cells were subjected to scRNA-seq using the 10X Chromium platform. Clustering analysis using the Louvain algorithm revealed distinct clusters representing major mesenchymal cell types, with a small proportion of hematopoietic and endothelial cells identified based on established markers (**Figure 4B; Figure S3A**). The major mesenchymal cell types present at the endosteum were osteoblasts, pre-osteoblasts, osteo-CAR, and adipo-CAR, as previously described [33]. Osteoblasts were defined by high expression of osteocalcin (*Bglap*), pre-osteoblasts by osteopontin (*Spp1*), osteo-CAR by LIM and calponin

homology domains 1 (*Limch1)*, adipo-CAR were identified by expression of C-X-C motif chemokine ligand 12 (*Cxcl12*), and osteocytes were identified by phosphate regulating endopeptidase X-linked (*Phex*) (**Figure 4C**). Although osteocytes are abundant in bone, they were not obtained in large numbers, likely due to their inefficient release from calcified bone matrix. It has been previously proposed that osteocytes mediate the deleterious effects of *Sod*2 deletion on bone mass [9]. However, due to the low numbers obtained, we could not perform a reliable analysis of the transcriptome of osteocytes lacking *Sod2*.

We first examined whether elevated ROS levels are associated with changes in the relative abundance of any of the clusters. Osteoblasts exhibited the most significant reduction in abundance with elevated ROS, decreasing from 35.3% to 20.5% (**Figure 4D**). This reduction is consistent with previous histomorphometric findings indicating that osteoblast number decreases upon *Sod2* deletion [34,35]. To identify changes in gene expression associated with elevated ROS in $Sod2^{\Delta Osx1}$ mice compared to controls, we performed differential expression analysis for each cell cluster using Model-based Analysis of Single-cell Transcriptomics (MAST) with a false discovery rate (FDR) < 0.05 and a random effect for sample origin [36]. In osteoblasts, we identified 575 differentially expressed genes (DEGs) (adjusted p < 0.05), among which 277 were upregulated and 298 downregulated (**Figure 4E**). Similarly, in adipo-CAR cells, we found 731 DEGs (adjusted p < 0.05), with 324 upregulated and 406 downregulated. Both pre-osteoblast and osteo-CAR exhibited fewer than 117 DEGs. As anticipated, cells from $Sod2^{\Delta Osx1}$ mice had altered oxidant detoxification genes. For example, glutathione peroxidase 4 (*Gpx4*), and glutathione S-transferases *Gstm1* and *Gstp1*, which detoxify lipid hydroperoxides, were all upregulated, as were metallothionein 1 and 2 (*Mt1 and Mt2*)

(**Figure 4F and 4G)**. Multiple transcription factors implicated in the response to oxidative stress, including BTB and CNC homology 1 *(Bach1*), Nuclear factor erythroid 2-related factor 2 (*Nfe2l2*), forkhead box O1 (*Foxo1*), and activating transcription factor 4 (*Atf4*) were also increased. In contrast, thioredoxins and ER-resident selenoproteins were downregulated (**Figure 4F).**

Sod2 deletion altered biological processes related to iron homeostasis and translation but not cellular senescence, in all major mesenchymal cell clusters

To identify biological processes impacted by *Sod2* deletion, we performed Gene Ontology (GO) enrichment analysis[37] (**Figure 5A**). Superoxide can damage proteins containing FeS clusters, such as aconitase [38-45], causing the release of ferrous iron and altered citrate metabolism [46]. Genes associated with iron sequestration and detoxification were upregulated, including the ferritin subunit *Ftl1* (**Figure 5B and 5C)** and heme oxygenase 1 (*Hmox1*), likely to mitigate Fenton-driven oxidative damage (**Figure 5B**). Genes related to rRNA processing, cytoplasmic translation, and mTOR signaling were also upregulated. These included genes encoding translation initiation factors such as *Eif1, Errfi1,* and *eIF4E* and numerous ribosomal proteins (**Figure 5B**). Genes related to several other cellular stress markers were upregulated, including angiogenesis, p38MAPK and p53 signaling.

ROS can promote senescence in osteoblastic cells *in vitro* [17] and *Sod2* deletion in mice can also cause cellular senescence [8]. Nonetheless, in our scRNAseq data, we found little evidence of cellular senescence. Of 119 senescence-related genes, compiled from SenMayo [47], MSigDB [48], and CellAge data sets [49], many of these

genes were downregulated in the Adipo-CAR cluster, and only a few, such as *Cdkn1a*, *Cdkn2a*, bone morphogenetic protein 2 (*Bmp2*) interleukin-6 (*Il6*), *Jun*, and vascular endothelial growth factor A (*Vegfa*,) were upregulated in the osteoblast cluster (**Figure S4A**). To further examine whether *Sod2* deletion could cause cellular senescence in our model, we cultured BMSCs from $Sod2^{\Delta Osx1}$ and Osx1-Cre control mice and found that the number of SA-β-gal-positive cells was not affected by *Sod2* deletion (**Figure 5D**). In contrast, an increase in the number of SA-β-Gal^{+} cells was easily seen when control cells were cultured in the presence of the DNA damaging drug etoposide, used here as a positive control. We also examined the expression of *Cdkn1a* and *Cdkn2a*, common markers of cellular senescence. The mRNA levels of *Cdkn1a* were decreased, and *Cdkn2a* was not different between cells from $Sod2^{\Delta Osx1}$ and Osx1-Cre control mice (**Figure 5E**). Finally, we examined expression of *Cdkn1a* and *Cdkn2a* in cortical bone shafts of femur, which contain osteocytes, osteoblast, and other mesenchymal lineage cells. An increase in *Cdkn2a* and other senescence markers is easily seen in bone shafts from old when compared to young wild-type mice [50,51]. However, we found no differences in expression of the two cell cycle inhibitors in bone from $Sod2^{\Delta Osx1}$ and Osx1-Cre mice (**Figure 5F**).

Sod2 deletion decreased expression of extracellular matrix and osteoblast differentiation genes

Deletion of *Sod2* downregulated cellular processes related to osteogenesis and extracellular matrix across all cell types (**Figure 6A**). The majority of bone matrix proteins are secreted by osteoblasts. Nonetheless, expression of type I collagen (*Col1a1*), the primary structural protein of bone matrix, was downregulated in all

clusters. Several other collagen genes were downregulated in osteoblasts from Sod2$^{\Delta Osx1}$ mice including *Col3a1, Col11a1, Coll11a2, Col5a1,* and *Col5a2* (**Figure 6B).** In addition, expression of protein disulfide isomerases (PDIs), including *Pdia3, Pdia4, and Pdia6*, essential for disulfide bond formation during protein folding in the ER, was decreased. Both calnexin (*Canx*) and calreticulin (*Calr*), which form a specific chaperone cycle for the biosynthesis of glycoproteins in the ER, were down-regulated, as was the collagen-specific chaperone heat shock protein 47 (Hsp47), encoded by *Serpinh1*, which stabilizes triple-helical procollagen and prevents lateral aggregation. The small leucine-rich repeat proteoglycan (SLRP) family is a group of proteins and proteoglycans that are found in the extracellular matrix and regulate matrix assembly and cell signaling. In Pre-osteoblasts, Osteo-CAR and Adipo-CAR, expression of SLRP members such as osteonectin (*Sparc*), decorin (*Dcn*), lumican (*Lum*), and osteomodulin (*Omd*) were downregulated. Osteo-CAR cells are thought to contain a long-lived osteoblast precursor population [33,52]. Osteo-CAR cells from Sod2$^{\Delta Osx1}$ mice had decreased expression of osteoblast differentiation markers such as *Alpl, Bglap,* and distal-less homeobox 5 (*Dlx5*). These cell types also had decreased expression of the parathyroid hormone receptor (*Pth1r*) (**Figure 6B and 6C)**. Parathyroid hormone (PTH) is a major stimulator of bone formation. Together with the decreased mineralization shown in **Figure 1F**, these data suggest that Sod2 deletion decreases extracellular matrix (ECM) production and osteoblast differentiation.

Osteoblasts lacking *Sod2* have decreased expression of genes implicated in collagen processing

We also noted that osteoblasts had decreased gene markers for protein folding and transport including tRNA aminoacylation and protein N-linked glycosylation (**Figure 6D and 6E)**. Specifically, aminoacyl-tRNA synthetases (aaRS), such as *Eprs, Tars, Rars, Gars,* and *Lars2*, responsible for covalently linking codons to their corresponding amino acids were decreased. Several prolyl and lysyl hydroxylases such as *P3h4, P4ha1, P4ha2,* and *P4hb,* as well as lysyl oxidase *Loxl2,* which is critical for stabilizing the collagen triple helix, were decreased in osteoblasts lacking Sod2 (**Figure 6D and 6E).** Components of the ER-to-Golgi transport machinery such as COPI complex subunits *Copa, Copb1, Copb2, Cope, Copg, Copz1,* and *Copz2,* as well as ER translocation components *Sec61a1, Sec61b, Sec63, Sec31c, Sec11c* were also downregulated. In line with a disruption in protein folding, the autophagy cargo markers p62 (*Sqstm1*) and microtubule-associated protein 1 light chain 3b (*Map1lc3b*) were upregulated, perhaps in an attempt to clear misfolded proteins (**Figure 6E)**. Several genes implicated in cellular metabolism were altered with Sod2 deletion. For example, the citrate transporter *Slc13a5*, which is highly expressed in osteoblasts[46], and the mitochondrial malate dehydrogenase (*Mdh2*) were downregulated, perhaps to avoid excessive accumulation of citrate due to inhibition of aconitase (**Figure 6D and 6E)**

Discussion

Cell type-specific knockout of *Sod2* in mice is a well-established approach for investigating specific effects of excessive mitochondrial ROS [53,54]. We show that deletion of *Sod2* in Osx1-Cre targeted cells caused low bone mass, associated with a decreased osteogenic potential of osteoblast lineage cells, consistent with findings

from previous studies using Runx2-Cre and Dmp1-Cre [8,9]. Importantly, our findings indicate that deletion of *Sod2* increases superoxide levels and reduces mitochondria respiration in osteoblastic cells mimicking some of the effects of aging. Deletion of *Sod2* also decreased the cellular levels of NAD^+ and supplementation with NR improved OCR in osteoblastic cells cultured from $Sod2^{\Delta Osx1}$ mice. However, NR administration did not alter the low bone mass of *Sod2* deficient mice, indicating that a decrease in NAD^+ is not a major mediator of the effects of mitochondrial ROS in bone cells. In contrast, administration of NR attenuates the loss of bone mass with aging[16]. Most likely, mechanisms other than ROS are predominantly responsible for the decline in NAD^+ with age.

Our scRNAseq analysis of mesenchymal lineage cells from bone of $Sod2^{\Delta Osx1}$ mice shed light on target cells and potential mechanisms responsible for the deleterious effects of excessive ROS in osteoblastic cells *in vivo*. Osteoblast precursors such as osteo-CAR and pre-osteoblasts had decreased expression of osteoblastic genes, suggesting decreased differentiation potential. These findings are in line with previous work suggesting that ROS inhibits osteoblast differentiation via FoxO transcription factors [55] and by oxidizing and degrading RUNX2 [56]. Interestingly, our single cell transcriptomic analysis revealed that osteoblast precursor cells from $Sod2^{\Delta Osx1}$ mice have lower expression of *Pth1r*. PTH is a critical regulator of blood calcium levels by promoting bone remodeling [57]. PTH signals through PTH1r, present in osteoblast lineage cells to stimulate both bone resorption and bone formation. Adult mice lacking *PTH1r* in osteoblast lineage cells exhibit accelerated bone loss with age, suggesting that PTH signaling protects mice from age-related bone loss [58]. Inhibition of salt-inducible kinases (SIKs) in osteoblasts and osteocytes is an important mediator of PTH actions on the skeleton [59,60]. In addition to the

decrease in *Pth1r* expression, Sod2$^{\Delta Osx1}$ mice exhibited an increase in *Sik1* expression in osteoblasts. Together, these findings suggest that a decrease in osteoblastic cell response to endogenous PTH might contribute to the inhibition of osteogenesis by ROS.

Mitochondrial ROS can diffuse to the endoplasmic reticulum, alter its redox environment and disrupt protein processing [61-65]. We identified changes in biological processes related to disrupted proteostasis in multiple cell clusters. Interestingly, osteoblasts were particularly impacted, most likely because of their major function of producing and secreting many bone matrix proteins. Collagen 1a, the primary structural protein of bone matrix, relies on a series of redox-dependent oxidative post-translational modifications for proper fibril formation and extracellular matrix integrity [66]. For example, the formation of disulfide bridges during protein folding is catalyzed by PDI and entails a redox reaction that leads to H_2O_2 generation. In *Sod2* knockout osteoblasts, several genes involved in these post-translational modifications such as PDIs, hydroxylases, PPIases, and chaperones, were downregulated, perhaps to curb a further increase in ROS. These findings are in line with recent evidence that ROS in growth plate chondrocytes inhibits PDI-mediated disulfide bridge formation, oxidative protein folding, ER proteostasis, and negatively affects matrix collagen properties [67]. Mice with connective tissue-specific *Sod2*-deficiecy also exhibited reduced collagen deposition and fibril thickness in the skin's dermis [68]. Accumulation of oxidative protein damage and a decline in proteostasis are closely linked to aging and age-related diseases [69-74]. Indeed, aged mice overexpressing mCAT maintain a youthful proteome in heart [75]. We have shown that targeted overexpression of the mCAT transgene in the mesenchymal lineage

attenuates age-related bone loss [7]. The capacity of mCAT to sustain proteostasis likely mitigates age-related pathologies, including bone loss.

Mitochondrial ROS has been causally implicated in cellular senescence [76-78]. Accordingly, *Sod2* deficiency induces DNA damage and promotes cellular senescence in some tissues [68,78]. Schoppa et al. have shown that deletion of *Sod2* in Runx2-expressing cells causes senescence which might contribute to the decreased bone formation [8]. Nonetheless, we found no markers of senescence in cultured osteoblastic cells, freshly isolated mesenchymal cells, or cortical bone from $Sod2^{\Delta Osx1}$ mice. While the reasons for this inconsistency remain unknown, it is possible that the age of the mice might contribute to the different results. Indeed, Schoppa et al. [8] reported an increase in cellular senescence in bone of 12-month-old mice, while our analysis was conducted in younger mice. Thus, deletion of *Sod2* might accelerate bone cell aging and increase the number of senescent cells at a time when these remain low in control mice. Alternatively, Runx2-Cre might target mesenchymal cells that are not targeted by Osx1-Cre, and these might become senescent with *Sod2* deletion. In any case, because the decrease in bone mass with *Sod2* deletion is seen as early as 3- month-of-age, it is unlikely that cellular senescence represents a major contributor to the decrease in bone mass. Thus, mitochondrial ROS might not represent major inducers of osteoblastic cell senescence with aging. This assumption aligns with observations that attenuation of mitochondrial ROS does not prevent cellular senescence in adipose tissue of aged mice [79].

Many aging-related pathologies, including loss of bone mass, are causally linked to ROS dysregulation. Nonetheless, the molecular mechanisms underlying these links are lacking. Work herein sheds light on oxidative stress-driven molecular changes in

osteoblastic lineage cells. Our findings suggest that mitochondrial ROS dysregulates protein homeostasis, particularly in osteoblasts. Future research should elucidate how changes in proteostasis alter bone mass. Our work also indicates that the loss of bone caused by excessive ROS is not mediated by changes in NAD^+ or cellular senescence, clarifying potential interconnections between these common mechanisms of aging. We propose that treatment combinations aimed at decreasing ROS, increasing NAD^+, and eliminating senescent cells might confer additive effects in delaying osteoporosis and reducing fracture risk with aging.

Resource availability

Lead contact

Further information and requests for resources and reagents should be directed to and will be fulfilled by the lead contact, Maria Almeida (schullermaria@uams.edu).

Materials availability

New unique materials were not generated in this study.

Data and Code Availability

- The scRNAseq datasets generated and/or analyzed during the current study are available in the NCBI Gene Expression Omnibus (GEO) repository under BioProject number PRJNA1231044.

- This paper does not report the original code.
- All other data generated or analyzed during this study are included in this published article and its supplementary information files.

Acknowledgments

The authors would like to thank Lee Ann MacMillan-Crow, Ph.D., for generously providing the cryopreserved Sod2 floxed ($^{f/f}$) mice and the CMDR Genetic Models Core for their assistance in retrieving them. We are grateful to the staff of the Bone Histology and Imaging Core and the UAMS Department of Laboratory Animal Medicine for their technical support. We also thank Olivia Reyes-Castro and Kimberly Richardson for their assistance with tissue collection. This work was supported by the US National Institutes of Health (R01AG068449, R01AR56679), Center for Musculoskeletal Disease Research COBRE (P20GM125503), and the UAMS Bone and Joint Initiative.

Author contributions

M.A. conceived the study. M.M.A., C.A.O., and M.A. designed experiments and analyzed the results. Q.F. recovered the Sod2 floxed ($^{f/f}$) mice from cryopreserved sperm. M.M.A. conducted the breeding of conditional *Sod2* knockout mice. M.M.A., A.R.C., and A.W. performed nicotinamide riboside (NR) administration studies. M.M.A. performed micro-CT measurements. M.M.A. and A.M.C. performed *in vitro* studies. H.N.K. provided technical support and discussed the results. C.A.O.

collected and processed samples for scRNA-seq. I.N., M.M.A., and M.A. analyzed the scRNA-seq data. M.M.A. and M.A. wrote the manuscript. All authors reviewed the manuscript.

Declaration of interests

The authors declare no competing interests.

Main figure titles and legends

Figure 1. Deletion of *Sod2* in osteoblast lineage cells causes low bone mass

(A) Quantitative RT-PCR analysis of *Sod2* mRNA expression levels in BMSCs cultured for 4 days (n = 5 mice/group).

(B) Bone mineral density (BMD) in 13-week-old female and 16-week-old male mice (*n* =9-10 mice/group).

(C and D) Quantitative µCT analysis of the femur and fifth lumbar vertebrae (*n* = 9-10 mice/group). Also see Figure S1

(E) mRNA expression levels of osteoblast marker genes in BMSCs cultured in triplicate for 7 days in osteogenic medium (n = 3 mice/group).

(F) BMSCs were cultured and incubated with 10 µM BrdU labeling for 48 hours (n = 3 mice/group). BMSCs subjected to serum starvation for 24 hours used as the control group.

(G) Alizarin red S staining of BMSCs after 21 days of culture in osteogenic medium. Representative images are shown on the left, with quantification on the right (n = 3 mice/group).

Data are means ± SD. P values by a two-tailed unpaired Student's t-test. (A–D) Each dot represents an individual mouse. (E-G) BMSCs from each group were pooled, and each dot represents an individual assay well.

Figure 2. Deletion of *Sod2* causes mitochondrial dysfunction mimicking the effects of aging in BMSCs

(A and D) Mitochondrial ROS (mtROS) levels in cultured BMSCs detected using the fluorescent probe 2.5 µM MitoSOX. (A) Control vs. $Sod2^{\Delta Osx1}$ (n = 6 mice/group). (D) Young vs. old (n = 3 mice/group).

(B and E) Mitochondrial membrane potential (ΔΨm) measured in cultured BMSCs (B) Control vs. $Sod2^{\Delta Osx1}$, measured with 2 µM JC-1 (red/green ratio; lower ratio = depolarization) (n = 6 mice/group). (E) Young vs. old, measured with 100 nM TMRM (lower fluorescence = lower ΔΨm) (n = 3 mice/group).

(C and F) Oxygen consumption rate (OCR) measured in live cultured BMSCs; right panels quantify basal and maximal mitochondrial respiration (C) Control vs. $Sod2^{\Delta Osx1}$ (n = 6 mice/group). (F) Young vs. old (n = 3 mice/group).

BMSCs from each group were pooled, and each dot represents an individual assay well. Data are means ± SD. P values by a two-tailed unpaired Student's t-test.

Figure 3. NR stimulates mitochondrial respiration in osteoblastic cell cultures but does not affect bone mass of Sod2$^{\Delta Osx1}$ mice

(A) Cellular NAD^+ levels in cultured BMSCs from control and Sod2$^{\Delta Osx1}$ mice (n = 6 mice/group).

(B) Oxygen consumption rate (OCR) in BMSCs after 16 h treatment with water (control) or 5mM NR. Oligo (oligomycin, an ATP synthase inhibitor), FCCP (carbonyl cyanide-4 (trifluoromethoxy) phenylhydrazone, an uncoupler of oxidative phosphorylation), and Rot & A (rotenone and antimycin A, inhibitors of complex I and III, respectively) were sequentially added to the cultures as indicated (n = 6 mice/group).

(C) Quantification of basal and maximal mitochondrial respiration from the OCR assays in (B).

(D) Schematic of *in vivo* NR supplementation in control and Sod2$^{\Delta Osx1}$ mice.

(E) Percentage change of lumbar spine and femoral BMD (n = 10-12 mice/group).

(F) Quantification of NAD^+ in white adipose tissue (n = 10-12 mice/group).

(G and H) Quantitative μCT analysis in (G) fifth lumbar vertebrae and (H) femur (n = 10-12 mice/group). See also Figure S2.

Data are mean ± SD. P-values by two-way ANOVA with Tukey's multiple comparisons test. (A-C) BMSCs from each group were pooled, and each dot represents an assay well. (E–H) Each dot represents an individual mouse.

Figure 4. scRNAseq reveals that Sod2 deletion greatly impacts the transcriptome of osteoblasts and adipo-CARs

(A) Schematic of endosteal mesenchymal cell isolation from femurs and tibias of 4-month-old male Sod2$^{\Delta Osx1}$ and control mice (n=1/group) enriched in mesenchymal lineage cells and subjected to scRNA-seq using the 10X Chromium platform.

(B) Uniform Manifold Approximation and Projection (UMAP) of endosteal mesenchymal cell clusters: Adipo-CAR, Osteo-CAR, preosteoblast (POB), osteoblast (OB), and osteocytes (OCY) identified by scRNA-seq. Each dot represents a single cell, color-coded by clusters. See Figure S3.

(C) Dot plot showing the expression of marker genes (*Cxcl12*, *Limch1*, *Spp1*, *Bglap*, *Phex*) across cell types. Dot size indicates the percentage of cells expressing the gene; color intensity represents the average expression level.

(D) Comparison of specific cell cluster proportions between Sod2$^{\Delta Osx1}$ and control mice. Numbers below the bars indicate the percentage of each cluster for each group.

(E) Distribution and directionality of differentially expressed genes (DEGs). Significant DEGs (p-adj < 0.05, red dots), with numbers of up/downregulated DEGs, are indicated above/below bars for each cell cluster.

(F) Log_2 fold change (Log_2FC) of antioxidant and stress response genes in OB clusters from Sod2$^{\Delta Osx1}$ compared to control.

(G) Violin plots of normalized expression levels of Gpx*4*, *Mt1* and *Mt2* in Adipo-CAR, Osteo-CAR, POB, and OB clusters from Sod2$^{\Delta Osx1}$ compared to control. Data are

box-and-whisker plots within the violins, (center line: median; box limits: 25th/75th percentiles; whiskers ±1.5× interquartile range).

Figure 5. *Sod2* deletion alters iron homeostasis and translation

(A) Dot plot displaying significantly upregulated Gene Ontology (GO) Biological Processes (P-adj < 0.05, gene count > 5). Larger circle sizes and darker colors indicate higher significance.

(B) Log_2FC of representative DEGs grouped by function (Iron homeostasis, Small ribosomal subunit, Large ribosomal subunit, Translation factors, and Angiogenesis & MAPK) in Adipo-CAR, Osteo-CAR, POB, and OB clusters from $Sod2^{\Delta Osx1}$ compared to control.

(C) Violin plots showing normalized expression of *Flt1*, *Rps6*, *Vegfa*, and *Gadd45b* in Adipo-CAR, Osteo-CAR, POB, and OB clusters from $Sod2^{\Delta Osx1}$ compared to control. Box-and-whisker plots (center line: median; box limits: 25th/75th percentiles; whiskers ±1.5× interquartile range)

(D) Quantification of SA-β-gal–positive BMSCs cultured in osteogenic medium for 4 days. Cells were pooled from each group (n = 3 mice/group) and plated in triplicate. Cells treated with etoposide (10 μM) used as a positive control.

(E and F) mRNA expression of *Cdkn2a* (p16) and *Cdkn1a* (p21) by qRT-PCR. (E) BMSCs were pooled from each mouse group (n = 3 mice/group) and cultured in triplicate in osteogenic medium for 7 days. (F) bone shafts (n = 5/group mice). See also Figure S4.

(D-F) Data are mean ± SD and P values by a two-tailed unpaired Student's t-test.

Figure 6. Osteoblasts with Sod2 deletion exhibit altered proteostasis

(A) Dot plot displaying significantly downregulated Gene Ontology (GO) Biological Processes (P-adj < 0.05, gene count > 5) in Adipo-CAR, Osteo-CAR, POB, and OB clusters from $Sod2^{\Delta Osx1}$ compared to control. Larger circle sizes and darker colors indicate higher significance.

(B) Log_2FC of representative DEGs grouped by folding and extracellular matrix (ECM) in Adipo-CAR, Osteo-CAR, POB, and OB clusters.

(C) Violin plots displaying the normalized expression of *Pth1r* in Adipo-CAR, Osteo-CAR, POB, and OB clusters from control and $Sod2^{\Delta Osx1}$ mice.

(D) Log_2FC of representative DEGs in OB clusters, grouped by aminoacyl-tRNA synthetases (aaRSs), protein folding and modification, ER-Golgi translocation and vesicular trafficking, and metabolism.

(E) Violin plots of normalized expression of *Tars, P4ha1, Golga4, Sqstm1,* and *Map1lc3b* significantly altered by Sod2 deletion in OB.

Data in (C and E) are box-and-whisker plots (center line: median; box limits: 25th/75th percentiles; whiskers ±1.5× interquartile range)

STAR Methods

Key resource table

REAGENT or RESOURCE	SOURCE	IDENTIFIER
Chemicals, peptides, and recombinant proteins		
Isoflurane solution	Piramal Critical Care	Cat# 6679401725
Etoposide	Calbiochem	Cat# 341205
X-gal	Sigma-Aldrich	Cat# B4252
Potassium ferrocyanide	Calbiochem	Cat# P3289
Potassium ferricyanide	Sigma-Aldrich	Cat# 702587
Sodium chloride	Sigma-Aldrich	Cat# BP358
Magnesium chloride	Thermo Fisher Scientific	Cat# M33
Sodium phosphate dibasic (Na_2HPO_4)	Thermo Fisher Scientific	Cat# S0876
10% Millonig's modified phosphate-buffered formalin	Leica Biosystems	Cat# 3800598
4% PFA	Thermo Fisher Scientific	Cat# 01176-014
Fetal Bovine Serum (FBS)	Gibco™	Cat# 10091155
Phosphate-Buffered Saline (PBS)	Gibco™	Cat#21600
Bovine serum albumin (BSA)	Gibco™	Cat# A7906
Antibiotics (Penicillin and Streptomycin)	Sigma-Aldrich	Cat# 15140122
Liberase TM	Roche	Cat# 5401119001
0.50% Trypsin, trypsin-EDTA	Gibco™	Cat# 15400054
B-glycerophosphate	Gibco™	Cat# G9422

Ascorbic acid	Sigma-Aldrich	Cat# A4403
Cetylpyridinium chloride	Sigma-Aldrich	Cat# C5560
Alizarin Red	Sigma-Aldrich	Cat# A5533
TRIzol reagent	Thermo Fisher Scientific	Cat# 15596026
HBSS, no calcium, no magnesium, no phenol red	Gibco™	Cat# 14175095
Seahorse XF base medium, without phenol red	Agilent Technologies	Cat# 103335-100
Seahorse XF 1.0 M Glucose Solution, 50 mL	Agilent Technologies	Cat#103577-100
Seahorse XF 100 mM Pyruvate Solution, 50 mL	Agilent Technologies	Cat#103578-100
Seahorse XF 200 mM Glutamine Solution, 50 mL	Agilent Technologies	Cat#103579-100
Seahorse XF Calibrant Solution 500 mL	Agilent Technologies	Cat #: 100840-000
MitoSOX™ Red	Thermo Fisher Scientific	Cat# M36008
JC-1 Dye (Mitochondrial Membrane Potential Probe)	Thermo Fisher Scientific	Cat# T3168
Tetramethylrhodamine, Methyl Ester, Perchlorate (TMRM)	Thermo Fisher Scientific	Cat# T668
Seahorse XF 200 mM Glutamine Solution, 50 mL	Agilent Technologies	Cat#103579-100

Critical Commercial Assays

REDExtract-N-Amp™ Tissue PCR Kit	Sigma-Aldrich	Cat# XNAT-100RXN
Cell Proliferation ELISA, BrdU (colorimetric)	Roche	Cat# 11647229001
Seahorse XF Cell Mito Stress Test Kit	Agilent Technologies	Cat#103015-100
EnzyFluo NAD/NADH Assay Kit	BioAssay Systems	Cat# EFND-100

High-Capacity cDNA Reverse Transcription Kit	Applied Biosystems	Cat# 4368813
TaqMan Universal PCR Master Mix	Applied Biosystems	Cat# 4304437
TaqMan™ Gene Expression Assay (FAM), mouse Cdkn1a	Thermo Fisher Scientific	Assay ID# Mm00432448_m1
TaqMan™ Gene Expression Assay (FAM), mouse *Cdkn2a*	Thermo Fisher Scientific	Assay ID# Mm00494449_m1
TaqMan™ Gene Expression Assay (FAM), mouse *Sod2*	Thermo Fisher Scientific	Assay ID# Mm00449726_m1
TaqMan™ Gene Expression Assay (FAM), mouse *Mrps2*	Thermo Fisher Scientific	Assay ID# Mm00475528_m1
Single Cell 3' Reagent Kits v3.1	10X Genomics	Cat# 1000128
Direct Lineage Cell Depletion Kit, mouse	Miltenyi Biotec	Cat# 130-090-858
CD45 MicroBeads, mouse	Miltenyi Biotec	Cat# 130-052-301
CD117 MicroBeads, mouse	Miltenyi Biotec	Cat# 130-091-224
CD31 MicroBeads, mouse	Miltenyi Biotec	Cat# 130-097-418
Invitrogen™ ReadyProbes™ Cell Viability Imaging Kit, Blue/Green	Thermo Fisher Scientific	Cat # R37609
Hoechst 33342, Trihydrochloride, Trihydrate - 10 mg/mL Solution in Water	Thermo Fisher Scientific	Cat# H3570
Deposited data		
Raw single-cell RNA sequencing data	This Paper	NCBI GEO: GSE232833
Experimental models: Organisms/strains		
Mouse: C57BL/6	Jackson Laboratory	Strain #:000664; RRID:IMSR_JAX:000664
$Sod2^{f/f}$ mice	Ikegami. *et al* [30]	From Lee Ann MacMillan-Crow (UAMS)

B6.Cg-Tg(Sp7-tTA,tetO-EGFP/cre)$^{1Amc/J}$	Jackson Laboratory	Strain # 006361; RRID:MGI:3689353
Oligonucleotides		
Primers for genotyping		
SOD2-P1:5 CGAGGGGCATCTAGTGGAGAAG;	Thermo Fisher Scientific	Cat# A15611
SOD2-P2:5 TTAGGGCTCAGGTTTGTCCATAA;	Thermo Fisher Scientific	Cat# A15611
CREgeno fwd:GCGGTCTGGCAGTAAAAACTATC;	Thermo Fisher Scientific	Cat# A15611
CREgeno rev: GTG AAACAGCATTGCTGTCACTT	Thermo Fisher Scientific	Cat# A15611
Software and Algorithms		
PIXImus densitometry	GE Healthcare Lunar Corp	N/A
MicroCT Systems	Scanco Medical AG	µCT40
QuantStudio 3 Real Time PCR System	Thermo Fisher Scientific	RRID: SCR_018712
GraphPad Prism 10	GraphPad Software Inc	https://www.graphpad.com/ RRID: SCR_002798
Seahorse Wave	Agilent Technologies	RRID:SCR_024491
BioRender	BioRender	http://biorender.com; RRID:SCR_018361
Adobe Illustrator	Adobe	https://www.adobe.com/products/illustrator.html; RRID: SCR_010279
cellSens Standard	Olympus	https://www.olympus-lifescience.com/en/software/cellsens/
ImageJ	NIH	https://imagej.nih.gov/ij/ RRID:SCR_003070
Image Lab Software	Bio-Rad	RRID:SCR_014210

Cell Ranger v7.2	Zheng et al. [80]	https://support.10xgenomics.com/single-cell-gene expression/software/pipelines/3.0/what-is-cell-ranger RRID:SCR_017344
Seurat v5	Stuart et al. [81]	https://satijalab.org/seurat/ RRID:SCR_016341
R Project for Statistical Computing	R project	https://www.r-project.org/; RRID: SCR_001905
MAST	Finak et al.[36]	RRID:SCR_016340
PIANO	Väremo et al. [82]	RRID:SCR_003200
Illumina NovaSeq 6000	Illumina	RRID:SCR_016387

Other

PicoLab®-5V5M	LabDiet	Cat# 3002909-703
PicoLab®-5V5R	LabDiet	Cat# 3002906-704
NR - Tru Niagen® 300mg Stick Packs	ChromaDex	Mfr Part # PHTN-SP001-30S-1
MACS® MultiStand	Miltenyi Biotec	Cat# 130-042-303
Agilent Seahorse XFe96 Analyzer	Agilent Technologies	RRID:SCR_019545
96-well Seahorse plates	Agilent Technologies	Cat #103794-100
Seahorse FluxPaks	Agilent Technologies	Cat #: 103792-100
96-well white-walled plates	Corning	Cat# 3917
96-well black walled plate	Corning	Cat # 3603
PCR Plate, 96-well, semi-skirted, flat deck	ThermoFisher Scientific	Cat # AB1400
Cell strainer (70∟µM)	Corning	Cat# 352350

Cytation 5 Cell Imaging Multi-Mode Reader	BioTek Instruments, Inc	RRID:SCR_019732
MACS® MultiStand	Miltenyi Biotec	Cat# 130-042-303
PTC-200 Thermal Cycler	MJ Research	RRID:SCR_025421
ChemiDoc XRS+ System	Bio-Rad	RRID:SCR_019690
MultiSample Bio-Pulverizer	BioSpec Products	Cat# 59012MS

Experimental model and subject details

Mice experiments

All animal procedures (protocol #AUP 4080(1)) were approved by the Institutional Animal Care and Use Committee (IACUC) of the University of Arkansas for Medical Sciences and conducted in compliance with the Public Health Service Policy, the NIH Guide for the Care and Use of Laboratory Animals (2011) [83], the AVMA Animal Euthanasia Guidelines (2020), and the ARRIVE guidelines 2.0 [84,85]. All experiments and methods were performed in accordance with these guidelines and regulations.

Male Sod2 floxed ($^{f/f}$) mice were obtained from cryopreserved sperm (provided by Lee Ann MacMillan-Crow at the University of Arkansas for Medical Sciences). Offspring from the *in vitro* fertilization (129/Sv and C57BL/6) were backcrossed to C57BL/6J mice (CD45.2) for four generations. Mice with conditional deletion of *Sod2* in osteoblast lineage cells were generated using a two-step breeding strategy. Hemizygous Osx1-cre transgenic mice (B6.Cg-Tg(Sp7-tTA,tetO-EGFP/cre)$^{1Amc/J}$; Jackson Laboratory, Strain# 006361) were crossed with Sod2$^{f/f}$ mice to produce offspring heterozygous for the floxed Sod2 allele with (Sod2$^{f/+}$; Osx1-cre) or without

($Sod2^{f/+}$) the Cre allele. These mice were intercrossed to generate $Sod2^{\Delta Osx1}$ and littermate controls (Osx1-cre) mice. Young (6 months) and old female (24 months) C57BL/6 mice were obtained (Jackson Laboratory, Strain# 000664) and acclimated for one week before harvest.

All mice were housed in groups of 2–5 animals per cage under controlled conditions (23°C, 60–70% humidity, 12-hour light/dark cycle), with *ad libitum* access to food and water. Breeder mice were fed the 5V5R diet (LabDiet, Cat. #3002906-704). All other mice were maintained on the 5V5M diet (LabDiet, Cat. #3002909-203). Body weight was measured before euthanasia. Mice were euthanized by CO_2 asphyxiation at designated time points, followed by cervical dislocation.

Bone marrow-derived stromal cell (BMSC) cultures

Total bone marrow cells were obtained by flushing the femurs and tibiae with isolation medium composed of α-Minimum Essential Medium (α-MEM) supplemented with 20% fetal bovine serum (FBS; Gibco™, Cat# 10091155) and 1% penicillin/streptomycin (PS; Gibco™, Cat# 15140122) [17]. Cells from 3-6 mice of each group were pooled, and red blood cells were removed using ACK buffer (0.01 mM EDTA, 0.011 M KHCO3, and 0.155 M NH4Cl, pH 7.3). The remaining cells were filtered through a 70 µM cell strainer (Corning, Cat# 352350) and cultured in 10-cm dishes for 7 days with α-MEM, 20% FBS, 1% PS, and 50 µg/mL ascorbic acid (Sigma-Aldrich, Cat# A4403). Cultures were maintained at 37°C in a humidified atmosphere containing 5% CO_2 and the medium was replaced every 3 days. Adherent stromal cells were detached using 0.5% trypsin-EDTA (Gibco™, Cat#

15400054) and re-plated for osteogenic differentiation or other downstream (mtROS, mt ΔΨm, Seahorse, NAD^+, SA-β-gal) assays.

Method details

Genotyping of transgenic mouse lines

All transgenic mouse colonies were genotyped by PCR using the REDExtract-N-Amp™ Tissue PCR Kit (Sigma-Aldrich, Cat# XNAT-100RXN) according to the manufacturer's instructions. Briefly, offspring were tail-clipped at weaning (21 days) and before sacrifice. Genomic DNA was extracted by incubating tail samples in extraction buffer for 10 minutes at room temperature, followed by heating at 95°C for 3 minutes and neutralization. Please note that during genotyping of Sod2 floxed mice, we determined that the neomycin phosphotransferase (neo) selection cassette that was contained in the original conditional allele was missing, likely due to an unintended recombination event. Sequencing of PCR products produced using primers P1 (5′-CGA GGG GCA TCT AGT GGA GAA G-3′) and P2 (5′-TTA GGG CTC AGG TTT GTC CAT AA-3′), product sizes = 500 bp for WT and 540 bp for the floxed allele, revealed that the 540 bp product contained the loxP site predicted to exist after recombination of the loxP sites flanking the neo cassette. PCR amplification of Osx1-cre was performed using primers CREgeno fwd (GCGGTCTGGCAGTAAAAACTATC) and CREgeno rev: GTG AAACAGCATTGCTGTCACTT. PCR products were separated on a 3% agarose gel and visualized using a ChemiDoc XRS+ Gel Imaging System (Bio-RAD).

Nicotinamide riboside (NR) administration

Female Sod2$^{\Delta Osx1}$ and littermate control mice were randomized based on BMD into vehicle or nicotinamide riboside (NR) treatment groups. 12 mM NR (ChromaDex, Mfr Part # PHTN-SP001-30S-1) was administered in filtered drinking water, provided *ad libitum* in light-protected bottles, and replaced every 2–3 days for four months.

Bone mineral density (BMD)

BMD was determined in mice using dual-energy X-ray absorptiometry (DEXA) with a PIXImus densitometer (GE Healthcare Lunar, software v2.0), as previously described [86]. Each scan had an acquisition time of 4 minutes and an analysis time of 6 minutes. Mice were sedated with 2% isoflurane to ensure they remained motionless during the scans. Spinal BMD was assessed using the L1–L6 vertebrae, and femoral BMD was determined from the entire right femur. Quality control, performed with a proprietary skeletal phantom, yielded a mean coefficient of variation below 2%. Vital signs (righting reflex, respiration, and heart rate) were monitored during sedation to facilitate rapid post-examination recovery.

Micro-computed tomography (μCT) scanning

Micro-computed tomography (μCT) was used to measure cortical and trabecular architecture of the fifth lumbar vertebra (L5) and right femur, as previously described [87,88]. L5 vertebra and femurs were dissected, cleaned of soft tissues, fixed in 10% Millonig's formalin (Leica Biosystems, Cat# 3800598) with 5% sucrose overnight, and gradually dehydrated in a graded series of ethanol (70%, 80%, 90%, and 100%)

at 4°C. Dehydrated bones were then loaded into a 12.3-mm-diameter scanning tube and scanned by a μCT (Scanco Biomedical, model# μCT40) to generate three-dimensional voxel images (1024 × 1024 pixels) of the bone samples. A Gaussian filter (sigma = 0.8, support = 1) was used to reduce signal noise, and a threshold of 200 was applied to all scans at medium resolution (E = 55 kVp, I = 145 μA, integration time = 200 ms). Bone parameters were measured using Scanco Eval Program v.6.0. For vertebral analysis, the entire L5 vertebral body was scanned, and cortical bone and primary spongiosa were manually excluded from the measurements. Trabecular measurements were made by drawing contours every 10–20 slices and using voxel counting for bone volume per tissue volume and sphere-filling distance transformation indices without presumptions about the bone shape as a rod or plate for trabecular microarchitecture. For femoral analysis, scanning was performed from a point immediately distal to the third trochanter down to the proximal edge of the distal growth plate. Cortical dimensions at the diaphysis were determined by analyzing 18 slices centered at the midpoint of the bone length as determined in scout view. Calibration and quality control were performed weekly using five density standards, and spatial resolution was verified monthly using a tungsten wire rod. Beam hardening correction was based on the calibration records. Image acquisition and analysis protocols adhered to the guidelines of the Journal of Bone and Mineral Research [89].

Osteogenic differentiation and alizarin red S staining

BMSCs were seeded in 12-well plates at a density of 2 × 10 cells/well in a medium containing 10% FBS, 1% penicillin-streptomycin (PS), and 50 μg/mL

ascorbic acid. After 2 days, osteogenic differentiation was induced by adding 10 mM β-glycerophosphate (Sigma-Aldrich, Cat# G9422), with media changes every 3 days.

On day 7 of osteogenic differentiation, total RNA was collected for RT-qPCR analysis of osteoblast-specific genes. Mineralization was assessed on day 21 using Alizarin Red S (AR-S) staining (Sigma-Aldrich, Cat# A5533). Briefly, cells were fixed in 10% Millonig's modified phosphate-buffered formalin for 30 minutes at room temperature. After two washes with double-distilled water (ddH_2O), cells were stained with 40 mM AR-S solution (pH 4.2) and incubated in the dark at room temperature for more than 20 minutes, followed by four washing steps with ddH_2O. After drying, the AR-S was destained with 10% cetylpyridinium chloride in 10 mM sodium phosphate (pH 7.0) (Sigma-Aldrich, Cat# C0732). The AR-S was quantified by absorbance measured at 562 nm against a known AR-S standard.

Cell proliferation assay

To evaluate BMSC proliferation, a BrdU incorporation assay was performed using a Cell Proliferation ELISA kit (Roche, Cat# 1647229) according to the manufacturer's instructions. Briefly, BMSCs (n = 5) were seeded at 4,000 cells per well in 96-well plates containing α-MEM supplemented with 10% FBS. At 60-70 % confluence, cells were incubated with 10 µM BrdU for 48 hours. The cells were then dried and fixed, and their DNA was denatured with FixDenat solution for 30 minutes at room temperature. Next, a peroxidase-conjugated mouse anti-BrdU monoclonal antibody was added and incubated for 90 minutes at room temperature. After washing, a tetramethylbenzidine substrate solution was applied for 15 minutes at room temperature, and absorbance was measured at 450–620 nm using a microplate

reader. Mean data were expressed as a ratio of the control (untreated) cell proliferation.

RNA isolation, cDNA synthesis, and quantitative RT–PCR

Right femoral and tibial bone shafts were prepared by removing bone ends, flushing marrow, and cleaning soft tissue and periosteum, as previously described [90]. The prepared shafts were then flash-frozen in liquid nitrogen and pulverized using a multi-well tissue pulverizer (BioSpec Products, Cat# 59012MS). Total RNA was extracted from pulverized bone and cultured cells using TRIzol reagent (Thermo Fisher Scientific, Cat# 15596026). For cells, a PBS wash preceded RNA extraction. Quantitation and determination of the 260/280 ratio of the extracted RNA were determined by NanoDrop™ 2000 spectrophotometer (Thermo Fisher Scientific). cDNA synthesis was performed from 1 µg of total RNA using the High-Capacity Reverse Transcription Kit (Applied Biosystems, Cat# 4368813) on a PTC-200 Peltier Thermal Cycler (MJ Research). Real-time qPCR was carried out using TaqMan™ Gene Expression Master Mix (Applied Biosystems, Cat# 4304437), gene-specific TaqMan™ probes, and primers *Sod2* (Mm00449726_m1); *Cdkn1a* (Mm00432448_m1); *Cdkn2a* (Mm00494449_m1)), on a Quant Studio 3 PCR System (Applied Biosystems; RRID:SCR_020238). Expression levels were normalized to the housekeeping gene *Mrps2* (Mm00475528_m1) and expressed as fold change using the $2^{\wedge-\Delta\Delta Ct}$ method [91].

Measurement of mitochondrial ROS

Mitochondrial superoxide (•O2−) levels were determined using the mitochondrial-specific probe MitoSOX™ Red (Thermo Fisher Scientific, Cat# M36008). Briefly, BMSCs were seeded at 2.0 × 10□ cells/well in the 96-well black-walled plate (Corning™, Cat# 3603) and cultured for 2 days in α-MEM supplemented with 10% FBS and 50 μg/mL ascorbic acid. Cells were washed twice with 1× PBS and incubated with 2.5 μM MitoSOX™ Red for 20 minutes at 37°C. Following two additional washes with PBS, fluorescence (Ex/Em = 510/580 nm) was measured using a Cytation 5 Cell Imaging Multi-Mode Reader (BioTek Instruments, Inc.; RRID:SCR_019732) to assess MitoSOX oxidation. MitoSOX intensity was normalized to nuclei counts using Hoechst 33342 (Thermo Fisher Scientific, Cat# H3570) staining.

Determination of mitochondrial membrane potential

Mitochondrial membrane potential (mt ΔΨm) in BMSCs from control & Sod2$^{\Delta Osx1}$was measured using the JC-1 Mitochondrial Membrane Potential Probe (Invitrogen™, Cat# T3168) according to the manufacturer's protocol. Briefly, BMSCs from control & Sod2$^{\Delta Osx1}$ mice were seeded at 2.0 × 10□ cells/well in 96-well black walled plate (Corning™, Cat# 3603) and cultured for 2 days in α-MEM supplemented with 10% FBS and 50 μg/mL ascorbic acid. Cells were washed twice with 1× PBS and incubated with 2 μM JC-1 for 15 minutes at 37°C. Following two additional washes with PBS, fluorescence (Ex/Em = 510/580 nm) was measured using a Cytation 5 Cell Imaging Multi-Mode Reader (BioTek Instruments, Inc.; RRID:SCR_019732). The ratio of JC-1 red to green fluorescence (Ex/Em ≈ 530/590□nm for red, 485/535□nm for green) was reported.

Mitochondrial membrane potential (mt ΔΨm) in BMSCs from young and old mice was measured using the tetramethylrhodamine (TMRM) probe (Invitrogen™, Cat# T668) according to the manufacturer's protocol. Briefly, BMSCs were seeded at 5 × 10□ cells/well in 96-well black-walled plates (Corning™, Cat#3 603) and cultured for 5 days in α-MEM with 50 µg/mL ascorbic acid. Following culture, cells were washed with PBS and incubated for 30 min at 37°C in assay medium (120 mM NaCl, 3.5 mM KCl, 5 mM $NaHCO_3$, 1.2 mM Na_2SO_4, 0.4 mM KH_2PO_4, 20 mM HEPES, 1.3 mM $CaCl_2$, 1.2 mM $MgCl_2$, 10 mM sodium pyruvate, pH 7.4) containing 100 nM TMRM. Fluorescence intensity (Ex/Em = 548/574 nm) was measured using a Cytation 5 Cell Imaging Multi-Mode Reader (BioTek Instruments, Inc.; RRID:SCR_019732) and normalized to cell counts using Hoechst 33342 staining.

Seahorse analysis

Oxygen consumption rates (OCR) were measured using Mito Stress Kit (Agilent Technologies Cat#103015-100) an XFe96 Seahorse Analyzer (Agilent Technologies; RRID:SCR_019545) following the manufacturer's protocol. BMSCs from control & $Sod2^{\Delta Osx1}$ mice were seeded at 4.0 × 10□ cells/well in 96-well Seahorse plates (Agilent Technologies, Cat# 103794-100) and cultured for 2 days in α-MEM supplemented with 10% FBS and 50 µg/mL ascorbic acid. For nicotinamide riboside (NR) treatment, 5mM NR was added with a media change on day 3, and cells were treated for an additional 16 hours. BMSCs from young & old mice were seeded at 4.0 × 10□ cells/well for 5 days in the same medium. Before the assay, cells were washed twice and incubated for 1 hour at 37°C (no CO_2) in 180 µl of Seahorse Base Medium (Agilent Technologies Cat# 103575) supplemented with 2

mM L-glutamine, 5.5 mM D-glucose, and 1 mM pyruvate. OCR was measured under basal conditions and after the sequential addition of 1.5 µM oligomycin, 2 µM FCCP, and 0.5 µM each of rotenone and antimycin A. Basal respiration was defined by the initial OCR values. Maximal respiration was calculated as FCCP-stimulated OCR minus OCR after rotenone/antimycin A treatment. Cells were stained with Hoechst 33342 (Thermo Fisher Scientific, Cat# H3570), counted using a Cytation 5 Cell Imaging Multi-Mode Reader (BioTek Instruments, Inc.; RRID:SCR_019732), and raw OCR values were normalized to the cell number. The data were analyzed using Wave Software (Agilent Technologies).

NAD^+ measurement

NAD^+ levels were measured in lysates from both fat tissue and BMSCs using the EnzyChrom™ NAD^+/NADH Assay Kit (Bioassay Systems, Cat# EFND-100) per manufacturer's instructions. Snap-frozen samples from control and $Sod2^{\Delta osx1\text{-}cre}$ mice were used directly for NAD^+ assay. Protein levels were quantified using the Bio-Rad colorimetric protein assay. BMSCs from control and $Sod2^{\Delta osx1\text{-}cre}$ mice were seeded at a density of 2×10^4 cells/well in 96-well white-walled plates (Corning™, Cat# 3917) and cultured for two days in α-MEM supplemented with 10% FBS and 50 µg/mL ascorbic acid.

Senescence-Associated β-Galactosidase (SA-β-gal) assay

BMSCs were seeded in six-well plates and cultured for two days. The medium was then replaced, and cells were treated with B-glycerophosphate (Gibco™, Cat#

G9422), while positive control groups received 10 µM etoposide (Calbiochem, Cat# 341205) for 3 days. Cells were washed with PBS and fixed with 4% paraformaldehyde (Sigma Aldrich, Cat# S0876) in PBS for 8 minutes, followed by two additional washes with PBS. For staining, the plates were incubated overnight (16–18 hours) at 37°C with a staining solution containing 1 mg/mL X-Gal (Sigma Aldrich, Cat# B4252), 40 mM citric acid/sodium phosphate buffer (pH 6.0), 5 mM potassium ferrocyanide (Calbiochem, Cat# 341205), 5 mM potassium ferricyanide (Sigma Aldrich, Cat# P3289), 150 mM sodium chloride, and 2 mM magnesium chloride (Fisher Scientific Cat# BP358). Following SA-β-gal staining, cells were counterstained with Hoechst dye (Thermo Fisher Scientific, Cat# H3570). Brightfield images were captured from at least three areas per well at 20× magnification using an inverted microscope (Olympus CKX41) equipped with a digital camera (Olympus DP20) and cellSens Standard software (Olympus Corp.). The same fields were imaged under the blue fluorescence channel to visualize Hoechst-stained nuclei. The proportion of SA-β-gal-positive cells was quantified using ImageJ software (NIH, RRID: SCR_002798)

Isolation of endosteal mesenchymal cells for scRNA-seq

Mesenchymal cells associated with the endosteal and trabecular bone surfaces were isolated from the femurs and tibias of 4-month-old $Sod2^{\Delta Osx1}$ and littermate control mice (n=1 per group), as described previously [33,51]. After euthanasia, femurs and tibias were cleaned of soft tissues, and the periosteum was removed by scraping with a scalpel. The epiphyses were excised, and bone shafts were cut longitudinally. Bone marrow was flushed using PBS supplemented with 1% bovine serum albumin

(BSA). The remaining bone fragments were then cut into smaller pieces of approximately 1 mm using a clean scalpel on a glass plate. Bone fragments were subjected to four Liberase™ (2 Wunsch units/mL in HBSS) and three EDTA (5 mM, 0.1% BSA in PBS without calcium or magnesium) digestions in a 6-well plate, alternating between the two solutions (20 min each, 37°C, 200 RPM). After each digestion, the cell-containing supernatant was collected and immediately placed on ice. Cells were then pelleted by centrifugation (300 x g, 10 min). The supernatants were carefully aspirated, leaving approximately 50-100 µL. Pellets were resuspended in 500 µL of sorting buffer (PBS, 0.5% BSA, 2 mM EDTA). Following the final digestion, all fractions were pooled, centrifuged, and resuspended in 100 µL of sorting buffer.

A two-step immunomagnetic depletion process using MACS column separation (Miltenyi Biote, Cat# 130-042-303) was used to enrich the mesenchymal cell population. First, a lineage cell depletion kit (Miltenyi Biotec, Cat# 130-090-858) was used to deplete hematopoietic and endothelial cells, following the manufacturer's instructions. Briefly, cells were incubated with a biotin-conjugated antibody cocktail, washed, and then incubated with anti-biotin microbeads. The cell suspension was then passed through an LS column, and the flow-through (lineage-negative fraction) was collected. To further deplete residual CD45+, CD117+, and CD31+ cells, the following microbeads were used: CD45 (Miltenyi Biotec, Cat# 130-052-301), CD117 (Miltenyi Biotec, Cat# 130-091-224), and CD31 (Miltenyi Biotec, Cat# 130-097-418). The cell suspension was incubated with each microbead set, washed, and then passed through a second LS column. The flow-through, containing the enriched endosteal mesenchymal cell population, was collected and filtered (70 µm, Corning™ Cat# 352350). Cells were then pelleted (300 x g, 10 min) and

resuspended in sorting buffer. Cells were then pelleted (300 x g, 10 min) and resuspended in sorting buffer. Cells were immediately transported at 4°C to the UAMS Genomics Core for single-cell RNA sequencing.

Single-cell RNA library preparation and sequencing

Single cells were stained with ReadyProbes Cell Viability Imaging Kit, Blue/Green (Thermo Fisher Scientific, Cat# R37609) and counted manually using a hemocytometer under an EVOS M7000 microscope (Thermo Fisher Scientific). Following cell counting, cells from each condition were encapsulated using a Chromium Controller (10X Genomics), and libraries were constructed using a Chromium Single Cell 3′ Reagent Kit (10X Genomics, PN-1000128) by the UAMS Genomics Core. Libraries were sequenced on an Illumina NovaSeq 6000 machine (RRID:SCR_016387) to generate FASTQ files.

Single-cell RNA-seq data processing and analysis

The bioinformatics analysis of the sc-RNAseq was followed our previous analysis of mesenchymal cells [33]. The FASTQ files were then preprocessed using Cell Ranger software version 7.2 (10X Genomics, RRID:SCR_017344) to produce feature-barcode matrices, with alignments conducted using the mouse reference genome mm10. These feature-barcode matrices were imported for further analysis into R software (RRID:SCR_016341), utilizing the Seurat package version 5 (RRID:SCR_016341) [81,92-94]. Cells containing between 1000 and 5,000 transcripts and mitochondria read content less than 15% were included in the analysis. The

samples were integrated to minimize batch effect using canonical correlation analysis (CCA) analysis is method with to 50 principle components, The cell clyster analysis was performed based on shared nearest neighbor modularity optimization based clustering algorithm of Louvain algorithm with multilevel refinement. Uniform Manifold Approximation and Projection (UMAP) dimensional reduction technique was performed for visualization of the results. Gene-specific markers for individual clusters and differentially expressed genes (DEGs) were identified using the MAST algorithm (RRID:SCR_016340), which has shown favorable results in recent benchmarks [33]. We used PIANO software (RRID:SCR_003200) to identify biological pathways and processes enriched in our sets of DEGs[82].

Quantification and statistical analysis

The statistical tests performed, number of replicates, and error measures for each experiment are indicated in the figure legends. Statistical analysis relating to scRNA-seq was performed in R software. Other statistical analyses were conducted in GraphPad Prism 10, following verification of data adherence to normality, equal variance, and independent sampling assumptions. Significance was defined as $p_{adj} \leq 0.05$ for GO terms and DEGs, and adjusted $p \leq 0.05$ for all other tests. Sample sizes for animal experiments were based on prior studies, and no data were excluded from analysis.

Additional resources

Figures were prepared using BioRender.com, Adobe Illustrator, and GraphPad Prism 10 (See **key resources table**).

Supplemental information

Document S1. Figures S1–S4

References

1. Borgstrom, F., Karlsson, L., Ortsater, G., Norton, N., Halbout, P., Cooper, C., Lorentzon, M., McCloskey, E.V., Harvey, N.C., Javaid, M.K., et al. (2020). Fragility fractures in Europe: burden, management and opportunities. Arch Osteoporos *15*, 59. 10.1007/s11657-020-0706-y.

2. Agarwal, A.R., Tarawneh, O., Cohen, J.S., Gu, A., Moseley, K.F., DeBritz, J.N., Golladay, G.J., and Thakkar, S.C. (2023). The incremental risk of fragility fractures in aging men. Osteoporos Int. 10.1007/s00198-023-06956-8.

3. Curtis, E.M., van der Velde, R., Moon, R.J., van den Bergh, J.P., Geusens, P., de Vries, F., van Staa, T.P., Cooper, C., and Harvey, N.C. (2016). Epidemiology of fractures in the United Kingdom 1988-2012: Variation with age, sex, geography, ethnicity and socioeconomic status. Bone *87*, 19-26. 10.1016/j.bone.2016.03.006.

4. Ensrud, K.E. (2013). Epidemiology of fracture risk with advancing age. J Gerontol A Biol Sci Med Sci *68*, 1236-1242. 10.1093/gerona/glt092.

5. Manolagas, S.C. (2010). From estrogen-centric to aging and oxidative stress: a revised perspective of the pathogenesis of osteoporosis. Endocr Rev *31*, 266-300. 10.1210/er.2009-0024.

6. Manolagas, S.C. (2000). Birth and death of bone cells: basic regulatory mechanisms and implications for the pathogenesis and treatment of osteoporosis. Endocr Rev *21*, 115-137. 10.1210/edrv.21.2.0395.

7. Ucer, S., Iyer, S., Kim, H.N., Han, L., Rutlen, C., Allison, K., Thostenson, J.D., de Cabo, R., Jilka, R.L., O'Brien, C., et al. (2017). The Effects of Aging and Sex Steroid Deficiency on the Murine Skeleton Are Independent and Mechanistically Distinct. J Bone Miner Res *32*, 560-574. 10.1002/jbmr.3014.

8. Schoppa, A.M., Chen, X., Ramge, J.M., Vikman, A., Fischer, V., Haffner-Luntzer, M., Riegger, J., Tuckermann, J., Scharffetter-Kochanek, K., and Ignatius, A. (2022). Osteoblast lineage Sod2 deficiency leads to an osteoporosis-like phenotype in mice. Dis Model Mech *15*. 10.1242/dmm.049392.

9. Kobayashi, K., Nojiri, H., Saita, Y., Morikawa, D., Ozawa, Y., Watanabe, K., Koike, M., Asou, Y., Shirasawa, T., Yokote, K., et al. (2015). Mitochondrial superoxide in osteocytes perturbs canalicular networks in the setting of age-related osteoporosis. Sci Rep *5*, 9148. 10.1038/srep09148.

10. Murphy, M.P. (2009). How mitochondria produce reactive oxygen species. Biochem J *417*, 1-13. 10.1042/BJ20081386.

11. Turrens, J.F. (2003). Mitochondrial formation of reactive oxygen species. J Physiol *552*, 335-344. 10.1113/jphysiol.2003.049478.

12. Cadenas, E., and Davies, K.J. (2000). Mitochondrial free radical generation, oxidative stress, and aging. Free Radic Biol Med *29*, 222-230. 10.1016/s0891-5849(00)00317-8.

13. Buettner, G.R. (2011). Superoxide dismutase in redox biology: the roles of superoxide and hydrogen peroxide. Anticancer Agents Med Chem *11*, 341-346. 10.2174/187152011795677544.

14. Lushchak, O.V., Piroddi, M., Galli, F., and Lushchak, V.I. (2014). Aconitase post-translational modification as a key in linkage between Krebs cycle, iron homeostasis, redox signaling, and metabolism of reactive oxygen species. Redox Rep *19*, 8-15. 10.1179/1351000213Y.0000000073.

15. Covarrubias, A.J., Perrone, R., Grozio, A., and Verdin, E. (2021). NAD(+) metabolism and its roles in cellular processes during ageing. Nat Rev Mol Cell Biol *22*, 119-141. 10.1038/s41580-020-00313-x.

16. Kim, H.N., Ponte, F., Warren, A., Ring, R., Iyer, S., Han, L., and Almeida, M. (2021). A decrease in NAD(+) contributes to the loss of osteoprogenitors and bone mass with aging. NPJ Aging Mech Dis *7*, 8. 10.1038/s41514-021-00058-7.

17. Kim, H.N., Xiong, J., MacLeod, R.S., Iyer, S., Fujiwara, Y., Cawley, K.M., Han, L., He, Y., Thostenson, J.D., Ferreira, E., et al. (2020). Osteocyte RANKL is required for cortical bone loss with age and is induced by senescence. JCI Insight *5*. 10.1172/jci.insight.138815.

18. Farr, J.N., Xu, M., Weivoda, M.M., Monroe, D.G., Fraser, D.G., Onken, J.L., Negley, B.A., Sfeir, J.G., Ogrodnik, M.B., Hachfeld, C.M., et al. (2017). Targeting cellular senescence prevents age-related bone loss in mice. Nat Med *23*, 1072-1079. 10.1038/nm.4385.

19. Gorgoulis, V., Adams, P.D., Alimonti, A., Bennett, D.C., Bischof, O., Bishop, C., Campisi, J., Collado, M., Evangelou, K., Ferbeyre, G., et al. (2019). Cellular Senescence: Defining a Path Forward. Cell *179*, 813-827. 10.1016/j.cell.2019.10.005.

20. Hayflick, L., and Moorhead, P.S. (1961). The serial cultivation of human diploid cell strains. Exp Cell Res *25*, 585-621. 10.1016/0014-4827(61)90192-6.

21. Campisi, J. (2013). Aging, cellular senescence, and cancer. Annu Rev Physiol *75*, 685-705. 10.1146/annurev-physiol-030212-183653 [doi].

22. Munoz-Espin, D., and Serrano, M. (2014). Cellular senescence: from physiology to pathology. Nat Rev Mol Cell Biol *15*, 482-496. nrm3823 [pii];10.1038/nrm3823 [doi].

23. Childs, B.G., Durik, M., Baker, D.J., and Van Deursen, J.M. (2015). Cellular senescence in aging and age-related disease: from mechanisms to therapy. Nat Med *21*, 1424-1435. nm.4000 [pii];10.1038/nm.4000 [doi].

24. Coppe, J.P., Patil, C.K., Rodier, F., Sun, Y., Munoz, D.P., Goldstein, J., Nelson, P.S., Desprez, P.Y., and Campisi, J. (2008). Senescence-associated secretory phenotypes reveal cell-nonautonomous functions of oncogenic RAS and the p53 tumor suppressor. PLoS Biol *6*, 2853-2868. 08-PLBI-RA-2566 [pii];10.1371/journal.pbio.0060301 [doi].

25. Coppe, J.P., Desprez, P.Y., Krtolica, A., and Campisi, J. (2010). The senescence-associated secretory phenotype: the dark side of tumor suppression. Annu Rev Pathol *5*, 99-118. 10.1146/annurev-pathol-121808-102144 [doi].

26. Kuilman, T., Michaloglou, C., Vredeveld, L.C., Douma, S., van, D.R., Desmet, C.J., Aarden, L.A., Mooi, W.J., and Peeper, D.S. (2008). Oncogene-induced senescence relayed by an interleukin-dependent inflammatory network. Cell *133*, 1019-1031. S0092-8674(08)00620-X [pii];10.1016/j.cell.2008.03.039 [doi].

27. Wajapeyee, N., Serra, R.W., Zhu, X., Mahalingam, M., and Green, M.R. (2008). Oncogenic BRAF induces senescence and apoptosis through pathways mediated by the secreted protein IGFBP7. Cell *132*, 363-374. S0092-8674(08)00053-6 [pii];10.1016/j.cell.2007.12.032 [doi].

28. Acosta, J.C., Banito, A., Wuestefeld, T., Georgilis, A., Janich, P., Morton, J.P., Athineos, D., Kang, T.W., Lasitschka, F., Andrulis, M., et al. (2013). A complex secretory program orchestrated by the inflammasome controls paracrine senescence. Nat Cell Biol *15*, 978-990. ncb2784 [pii];10.1038/ncb2784 [doi].

29. Rodda, S.J., and McMahon, A.P. (2006). Distinct roles for Hedgehog and canonical Wnt signaling in specification, differentiation and maintenance of osteoblast progenitors. Development *133*, 3231-3244. 10.1242/dev.02480.

30. Ikegami, T., Suzuki, Y., Shimizu, T., Isono, K., Koseki, H., and Shirasawa, T. (2002). Model mice for tissue-specific deletion of the manganese superoxide dismutase (MnSOD) gene. Biochem Biophys Res Commun *296*, 729-736. 10.1016/s0006-291x(02)00933-6.

31. Massudi, H., Grant, R., Braidy, N., Guest, J., Farnsworth, B., and Guillemin, G.J. (2012). Age-associated changes in oxidative stress and NAD+ metabolism in human tissue. PLoS One *7*, e42357. 10.1371/journal.pone.0042357.

32. Verdin, E. (2015). NAD(+) in aging, metabolism, and neurodegeneration. Science *350*, 1208-1213. 10.1126/science.aac4854.

33. Nookaew, I., Xiong, J., Onal, M., Bustamante-Gomez, C., Wanchai, V., Fu, Q., Kim, H.N., Almeida, M., and O'Brien, C.A. (2024). Refining the identity of mesenchymal cell types associated with murine periosteal and endosteal bone. J Biol Chem *300*, 107158. 10.1016/j.jbc.2024.107158.

34. Almeida, M., Han, L., Martin-Millan, M., Plotkin, L.I., Stewart, S.A., Roberson, P.K., Kousteni, S., O'Brien, C.A., Bellido, T., Parfitt, A.M., et al. (2007). Skeletal involution by age-associated oxidative stress and its acceleration by loss of sex steroids. J Biol. Chem *282*, 27285-27297.

35. Ucer, S., Iyer, S., Kim, H.N., Han, L., Rutlen, C., Allison, K., Thostenson, J.D., de, C.R., Jilka, R.L., O'Brien, C., et al. (2017). The Effects of Aging and Sex Steroid Deficiency on the Murine Skeleton Are Independent and Mechanistically Distinct. J Bone Miner Res *32*, 560-574. 10.1002/jbmr.3014 [doi].

36. Finak, G., McDavid, A., Yajima, M., Deng, J., Gersuk, V., Shalek, A.K., Slichter, C.K., Miller, H.W., McElrath, M.J., Prlic, M., et al. (2015). MAST: a flexible statistical framework for assessing transcriptional changes and characterizing heterogeneity in single-cell RNA sequencing data. Genome Biol *16*, 278. 10.1186/s13059-015-0844-5.

37. Ashburner, M., Ball, C.A., Blake, J.A., Botstein, D., Butler, H., Cherry, J.M., Davis, A.P., Dolinski, K., Dwight, S.S., Eppig, J.T., et al. (2000). Gene ontology: tool for the unification of biology. The Gene Ontology Consortium. Nat Genet *25*, 25-29. 10.1038/75556.

38. Gardner, P.R., Raineri, I., Epstein, L.B., and White, C.W. (1995). Superoxide radical and iron modulate aconitase activity in mammalian cells. J Biol Chem *270*, 13399-13405. 10.1074/jbc.270.22.13399.

39. Bhattacharya, A., Lustgarten, M., Shi, Y., Liu, Y., Jang, Y.C., Pulliam, D., Jernigan, A.L., and Van Remmen, H. (2011). Increased mitochondrial matrix-directed superoxide production by fatty acid hydroperoxides in skeletal muscle mitochondria. Free Radic Biol Med *50*, 592-601. 10.1016/j.freeradbiomed.2010.12.014.

40. Li, Y., Huang, T.T., Carlson, E.J., Melov, S., Ursell, P.C., Olson, J.L., Noble, L.J., Yoshimura, M.P., Berger, C., Chan, P.H., et al. (1995). Dilated cardiomyopathy and neonatal lethality in mutant mice lacking manganese superoxide dismutase. Nat Genet *11*, 376-381. 10.1038/ng1295-376.

41. Lustgarten, M.S., Jang, Y.C., Liu, Y., Qi, W., Qin, Y., Dahia, P.L., Shi, Y., Bhattacharya, A., Muller, F.L., Shimizu, T., et al. (2011). MnSOD deficiency results in elevated oxidative stress and decreased mitochondrial function but does not lead to muscle atrophy during aging. Aging Cell *10*, 493-505. 10.1111/j.1474-9726.2011.00695.x.

42. Melov, S., Coskun, P., Patel, M., Tuinstra, R., Cottrell, B., Jun, A.S., Zastawny, T.H., Dizdaroglu, M., Goodman, S.I., Huang, T.T., et al. (1999). Mitochondrial disease in

superoxide dismutase 2 mutant mice. Proc Natl Acad Sci U S A *96*, 846-851. 10.1073/pnas.96.3.846.

43. Jones, M.K., Zhu, E., Sarino, E.V., Padilla, O.R., Takahashi, T., Shimizu, T., and Shirasawa, T. (2011). Loss of parietal cell superoxide dismutase leads to gastric oxidative stress and increased injury susceptibility in mice. Am J Physiol Gastrointest Liver Physiol *301*, G537-546. 10.1152/ajpgi.00177.2011.

44. Ahn, B., Ranjit, R., Premkumar, P., Pharaoh, G., Piekarz, K.M., Matsuzaki, S., Claflin, D.R., Riddle, K., Judge, J., Bhaskaran, S., et al. (2019). Mitochondrial oxidative stress impairs contractile function but paradoxically increases muscle mass via fibre branching. J Cachexia Sarcopenia Muscle *10*, 411-428. 10.1002/jcsm.12375.

45. Ostrom, E.L., Stuppard, R., Mattson-Hughes, A., and Marcinek, D.J. (2024). Inducible and reversible SOD2 knockdown in mouse skeletal muscle drives impaired pyruvate oxidation and reduced metabolic flexibility. bioRxiv. 10.1101/2024.09.23.614547.

46. Dirckx, N., Zhang, Q., Chu, E.Y., Tower, R.J., Li, Z., Guo, S., Yuan, S., Khare, P.A., Zhang, C., Verardo, A., et al. (2022). A specialized metabolic pathway partitions citrate in hydroxyapatite to impact mineralization of bones and teeth. Proc Natl Acad Sci U S A *119*, e2212178119. 10.1073/pnas.2212178119.

47. Saul, D., Kosinsky, R.L., Atkinson, E.J., Doolittle, M.L., Zhang, X., LeBrasseur, N.K., Pignolo, R.J., Robbins, P.D., Niedernhofer, L.J., Ikeno, Y., et al. (2022). A new gene set identifies senescent cells and predicts senescence-associated pathways across tissues. Nat Commun *13*, 4827. 10.1038/s41467-022-32552-1.

48. Liberzon, A., Birger, C., Thorvaldsdottir, H., Ghandi, M., Mesirov, J.P., and Tamayo, P. (2015). The Molecular Signatures Database (MSigDB) hallmark gene set collection. Cell Syst *1*, 417-425. 10.1016/j.cels.2015.12.004.

49. Avelar, R.A., Ortega, J.G., Tacutu, R., Tyler, E.J., Bennett, D., Binetti, P., Budovsky, A., Chatsirisupachai, K., Johnson, E., Murray, A., et al. (2020). A multidimensional systems biology analysis of cellular senescence in aging and disease. Genome Biol *21*, 91. 10.1186/s13059-020-01990-9.

50. Piemontese, M., Almeida, M., Robling, A.G., Kim, H.N., Xiong, J., Thostenson, J.D., Weinstein, R.S., Manolagas, S.C., O'Brien, C.A., and Jilka, R.L. (2017). Old age causes de novo intracortical bone remodeling and porosity in mice. JCI Insight *2*. 10.1172/jci.insight.93771.

51. Farr, J.N., Fraser, D.G., Wang, H., Jaehn, K., Ogrodnik, M.B., Weivoda, M.M., Drake, M.T., Tchkonia, T., LeBrasseur, N.K., Kirkland, J.L., et al. (2016). Identification of Senescent Cells in the Bone Microenvironment. J Bone Miner Res *31*, 1920-1929. 10.1002/jbmr.2892.

52. Baccin, C., Al-Sabah, J., Velten, L., Helbling, P.M., Grunschlager, F., Hernandez-Malmierca, P., Nombela-Arrieta, C., Steinmetz, L.M., Trumpp, A., and Haas, S. (2020). Combined single-cell and spatial transcriptomics reveal the molecular, cellular and spatial bone marrow niche organization. Nat Cell Biol *22*, 38-48. 10.1038/s41556-019-0439-6.

53. Misawa, H., Nakata, K., Matsuura, J., Moriwaki, Y., Kawashima, K., Shimizu, T., Shirasawa, T., and Takahashi, R. (2006). Conditional knockout of Mn superoxide dismutase in postnatal motor neurons reveals resistance to mitochondrial generated superoxide radicals. Neurobiol Dis *23*, 169-177. 10.1016/j.nbd.2006.02.014.

54. Shimizu, T., Nojiri, H., Kawakami, S., Uchiyama, S., and Shirasawa, T. (2010). Model mice for tissue-specific deletion of the manganese superoxide dismutase gene. Geriatr Gerontol Int *10 Suppl 1*, S70-79. 10.1111/j.1447-0594.2010.00604.x.

55. Iyer, S., Ambrogini, E., Bartell, S.M., Han, L., Roberson, P.K., de Cabo, R., Jilka, R.L., Weinstein, R.S., O'Brien, C.A., Manolagas, S.C., and Almeida, M. (2013).

FOXOs attenuate bone formation by suppressing Wnt signaling. J Clin Invest *123*, 3409-3419. 10.1172/JCI68049.

56. Hu, G., Yu, Y., Sharma, D., Pruett-Miller, S.M., Ren, Y., Zhang, G.F., and Karner, C.M. (2023). Glutathione limits RUNX2 oxidation and degradation to regulate bone formation. JCI Insight *8*. 10.1172/jci.insight.166888.

57. Wein, M.N., and Kronenberg, H.M. (2018). Regulation of Bone Remodeling by Parathyroid Hormone. Cold Spring Harb Perspect Med *8*. 10.1101/cshperspect.a031237.

58. Uda, Y., Saini, V., Petty, C.A., Alshehri, M., Shi, C., Spatz, J.M., Santos, R., Newell, C.M., Huang, T.Y., Kochen, A., et al. (2021). Parathyroid hormone signaling in mature osteoblasts/osteocytes protects mice from age-related bone loss. Aging (Albany NY) *13*, 25607-25642. 10.18632/aging.203808.

59. Nishimori, S., O'Meara, M.J., Castro, C.D., Noda, H., Cetinbas, M., da Silva Martins, J., Ayturk, U., Brooks, D.J., Bruce, M., Nagata, M., et al. (2019). Salt-inducible kinases dictate parathyroid hormone 1 receptor action in bone development and remodeling. J Clin Invest *129*, 5187-5203. 10.1172/JCI130126.

60. Wein, M.N., Liang, Y., Goransson, O., Sundberg, T.B., Wang, J., Williams, E.A., O'Meara, M.J., Govea, N., Beqo, B., Nishimori, S., et al. (2016). SIKs control osteocyte responses to parathyroid hormone. Nat Commun *7*, 13176. 10.1038/ncomms13176.

61. Mannaa, A., and Hanisch, F.G. (2020). Redox Proteomes in Human Physiology and Disease Mechanisms. J Proteome Res *19*, 1-17. 10.1021/acs.jproteome.9b00586.

62. Sies, H., Mailloux, R.J., and Jakob, U. (2024). Fundamentals of redox regulation in biology. Nat Rev Mol Cell Biol *25*, 701-719. 10.1038/s41580-024-00730-2.

63. Urrutia, P.J., and Borquez, D.A. (2023). Expanded bioinformatic analysis of Oximouse dataset reveals key putative processes involved in brain aging and cognitive decline. Free Radic Biol Med *207*, 200-211. 10.1016/j.freeradbiomed.2023.07.018.

64. Day, N.J., Kelly, S.S., Lui, L.Y., Mansfield, T.A., Gaffrey, M.J., Trejo, J.B., Sagendorf, T.J., Attah, I.K., Moore, R.J., Douglas, C.M., et al. (2024). Signatures of cysteine oxidation on muscle structural and contractile proteins are associated with physical performance and muscle function in older adults: Study of Muscle, Mobility and Aging (SOMMA). Aging Cell *23*, e14094. 10.1111/acel.14094.

65. Jonak, K., Suppanz, I., Bender, J., Chacinska, A., Warscheid, B., and Topf, U. (2024). Ageing-dependent thiol oxidation reveals early oxidation of proteins with core proteostasis functions. Life Sci Alliance *7*. 10.26508/lsa.202302300.

66. Claeys, L., Storoni, S., Eekhoff, M., Elting, M., Wisse, L., Pals, G., Bravenboer, N., Maugeri, A., and Micha, D. (2021). Collagen transport and related pathways in Osteogenesis Imperfecta. Hum Genet *140*, 1121-1141. 10.1007/s00439-021-02302-2.

67. Loopmans, S., Rohlenova, K., van Brussel, T., Stockmans, I., Moermans, K., Peredo, N., Carmeliet, P., Lambrechts, D., Stegen, S., and Carmeliet, G. (2025). The pentose phosphate pathway controls oxidative protein folding and prevents ferroptosis in chondrocytes. Nat Metab *7*, 182-195. 10.1038/s42255-024-01187-5.

68. Treiber, N., Maity, P., Singh, K., Kohn, M., Keist, A.F., Ferchiu, F., Sante, L., Frese, S., Bloch, W., Kreppel, F., et al. (2011). Accelerated aging phenotype in mice with conditional deficiency for mitochondrial superoxide dismutase in the connective tissue. Aging Cell *10*, 239-254. 10.1111/j.1474-9726.2010.00658.x.

69. Hipp, M.S., Kasturi, P., and Hartl, F.U. (2019). The proteostasis network and its decline in ageing. Nat Rev Mol Cell Biol *20*, 421-435. 10.1038/s41580-019-0101-y.

70. Labbadia, J., and Morimoto, R.I. (2015). The biology of proteostasis in aging and disease. Annu Rev Biochem *84*, 435-464. 10.1146/annurev-biochem-060614-033955.

71. Klaips, C.L., Jayaraj, G.G., and Hartl, F.U. (2018). Pathways of cellular proteostasis in aging and disease. J Cell Biol *217*, 51-63. 10.1083/jcb.201709072.

72. Taylor, R.C., and Dillin, A. (2011). Aging as an event of proteostasis collapse. Cold Spring Harb Perspect Biol *3*. 10.1101/cshperspect.a004440.

73. Kaushik, S., and Cuervo, A.M. (2015). Proteostasis and aging. Nat Med *21*, 1406-1415. 10.1038/nm.4001.

74. Ulfig, A., and Jakob, U. (2024). Cellular oxidants and the proteostasis network: balance between activation and destruction. Trends Biochem Sci *49*, 761-774. 10.1016/j.tibs.2024.07.001.

75. Basisty, N., Dai, D.F., Gagnidze, A., Gitari, L., Fredrickson, J., Maina, Y., Beyer, R.P., Emond, M.J., Hsieh, E.J., MacCoss, M.J., et al. (2016). Mitochondrial-targeted catalase is good for the old mouse proteome, but not for the young: 'reverse' antagonistic pleiotropy? Aging Cell *15*, 634-645. 10.1111/acel.12472.

76. Passos, J.F., Nelson, G., Wang, C., Richter, T., Simillion, C., Proctor, C.J., Miwa, S., Olijslagers, S., Hallinan, J., Wipat, A., et al. (2010). Feedback between p21 and reactive oxygen production is necessary for cell senescence. Mol Syst Biol *6*, 347. 10.1038/msb.2010.5.

77. Moiseeva, O., Bourdeau, V., Roux, A., Deschenes-Simard, X., and Ferbeyre, G. (2009). Mitochondrial dysfunction contributes to oncogene-induced senescence. Mol Cell Biol *29*, 4495-4507. 10.1128/MCB.01868-08.

78. Velarde, M.C., Flynn, J.M., Day, N.U., Melov, S., and Campisi, J. (2012). Mitochondrial oxidative stress caused by Sod2 deficiency promotes cellular

senescence and aging phenotypes in the skin. Aging (Albany NY) *4*, 3-12. 10.18632/aging.100423.

79. Mogck, B.A., Jezak, S.T., and Wiley, C.D. (2024). Mitochondria-Targeted Catalase Does Not Suppress Development of Cellular Senescence during Aging. Biomedicines *12*. 10.3390/biomedicines12020414.

80. Zheng, G.X., Terry, J.M., Belgrader, P., Ryvkin, P., Bent, Z.W., Wilson, R., Ziraldo, S.B., Wheeler, T.D., McDermott, G.P., Zhu, J., et al. (2017). Massively parallel digital transcriptional profiling of single cells. Nat Commun *8*, 14049. 10.1038/ncomms14049.

81. Stuart, T., Butler, A., Hoffman, P., Hafemeister, C., Papalexi, E., Mauck, W.M., 3rd, Hao, Y., Stoeckius, M., Smibert, P., and Satija, R. (2019). Comprehensive Integration of Single-Cell Data. Cell *177*, 1888-1902 e1821. 10.1016/j.cell.2019.05.031.

82. Varemo, L., Nielsen, J., and Nookaew, I. (2013). Enriching the gene set analysis of genome-wide data by incorporating directionality of gene expression and combining statistical hypotheses and methods. Nucleic Acids Res *41*, 4378-4391. 10.1093/nar/gkt111.

83. (2011). In Guide for the Care and Use of Laboratory Animals. 10.17226/12910.

84. Percie du Sert, N., Hurst, V., Ahluwalia, A., Alam, S., Avey, M.T., Baker, M., Browne, W.J., Clark, A., Cuthill, I.C., Dirnagl, U., et al. (2020). The ARRIVE guidelines 2.0: updated guidelines for reporting animal research. BMJ Open Sci *4*, e100115. 10.1136/bmjos-2020-100115.

85. Percie du Sert, N., Ahluwalia, A., Alam, S., Avey, M.T., Baker, M., Browne, W.J., Clark, A., Cuthill, I.C., Dirnagl, U., Emerson, M., et al. (2020). Reporting animal research: Explanation and elaboration for the ARRIVE guidelines 2.0. PLoS Biol *18*, e3000411. 10.1371/journal.pbio.3000411.

86. Bartell, S.M., Kim, H.N., Ambrogini, E., Han, L., Iyer, S., Serra Ucer, S., Rabinovitch, P., Jilka, R.L., Weinstein, R.S., Zhao, H., et al. (2014). FoxO proteins restrain osteoclastogenesis and bone resorption by attenuating H2O2 accumulation. Nat Commun *5*, 3773. 10.1038/ncomms4773.

87. Resende-Coelho, A., Ali, M.M., James, A., Warren, A., Gatrell, L., Kadhim, I., Fu, Q., Xiong, J., Onal, M., and Almeida, M. (2025). Mitochondrial oxidative stress or decreased autophagy in osteoblast lineage cells is not sufficient to mimic the deleterious effects of aging on bone mechanoresponsiveness. Aging (Albany NY) *17*. 10.18632/aging.206213.

88. Warren, A., Porter, R.M., Reyes-Castro, O., Ali, M.M., Marques-Carvalho, A., Kim, H.N., Gatrell, L.B., Schipani, E., Nookaew, I., O'Brien, C.A., et al. (2023). The NAD salvage pathway in mesenchymal cells is indispensable for skeletal development in mice. Nat Commun *14*, 3616. 10.1038/s41467-023-39392-7.

89. Dempster, D.W., Compston, J.E., Drezner, M.K., Glorieux, F.H., Kanis, J.A., Malluche, H., Meunier, P.J., Ott, S.M., Recker, R.R., and Parfitt, A.M. (2013). Standardized nomenclature, symbols, and units for bone histomorphometry: a 2012 update of the report of the ASBMR Histomorphometry Nomenclature Committee. J Bone Miner Res *28*, 2-17. 10.1002/jbmr.1805.

90. Xiong, J., Onal, M., Jilka, R.L., Weinstein, R.S., Manolagas, S.C., and O'Brien, C.A. (2011). Matrix-embedded cells control osteoclast formation. Nat Med *17*, 1235-1241. 10.1038/nm.2448.

91. Livak, K.J., and Schmittgen, T.D. (2001). Analysis of relative gene expression data using real-time quantitative PCR and the 2(-Delta Delta C(T)) Method. Methods *25*, 402-408. 10.1006/meth.2001.1262.

92. Hao, Y., Hao, S., Andersen-Nissen, E., Mauck, W.M., 3rd, Zheng, S., Butler, A., Lee, M.J., Wilk, A.J., Darby, C., Zager, M., et al. (2021). Integrated analysis of multimodal single-cell data. Cell *184*, 3573-3587.e3529. 10.1016/j.cell.2021.04.048.

93. Hafemeister, C., and Satija, R. (2019). Normalization and variance stabilization of single-cell RNA-seq data using regularized negative binomial regression. Genome Biol *20*, 296. 10.1186/s13059-019-1874-1.

94. Hao, Y., Hao, S., Andersen-Nissen, E., Mauck, W.M., 3rd, Zheng, S., Butler, A., Lee, M.J., Wilk, A.J., Darby, C., Zager, M., et al. (2021). Integrated analysis of multimodal single-cell data. Cell *184*, 3573-3587 e3529. 10.1016/j.cell.2021.04.048.

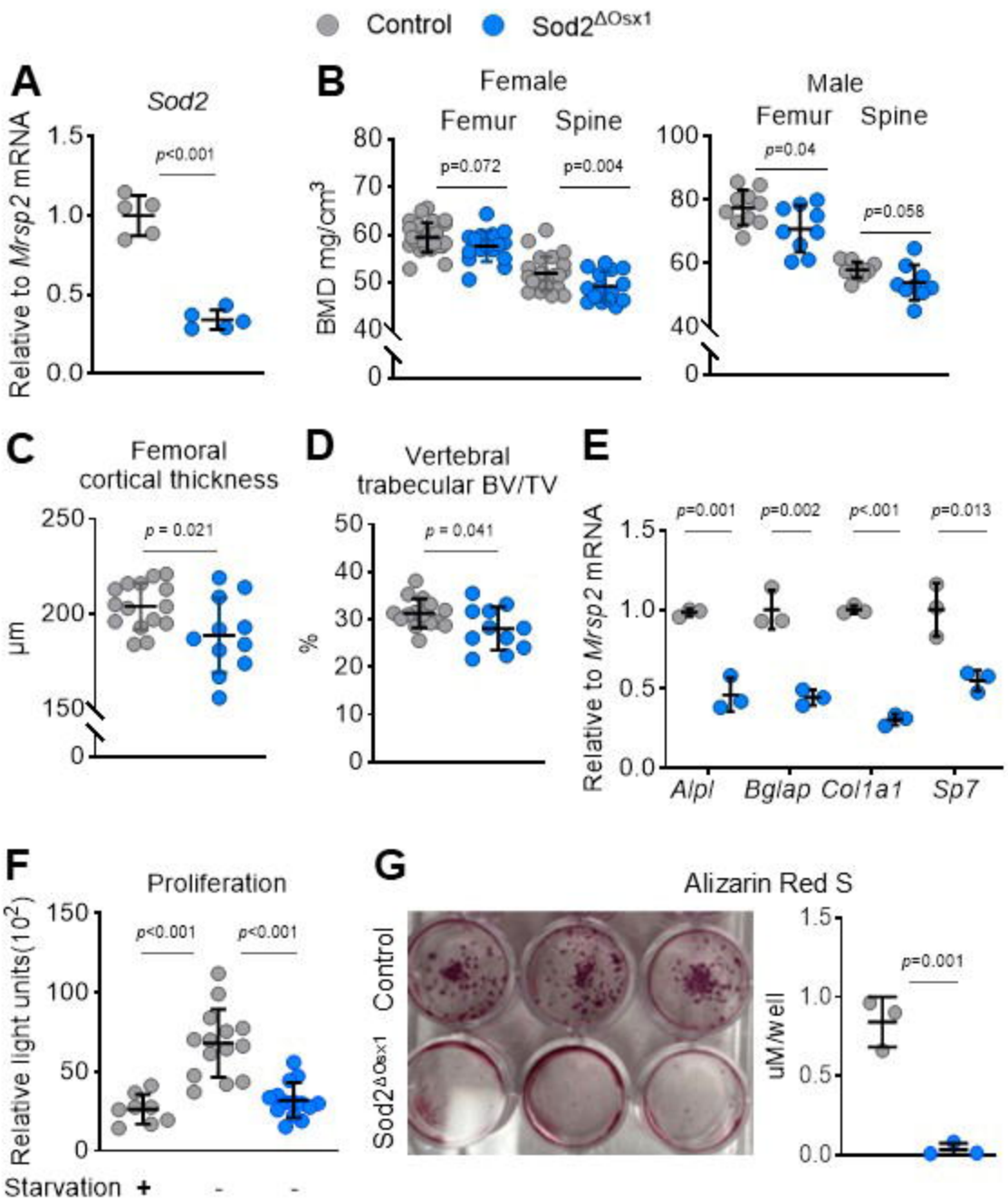

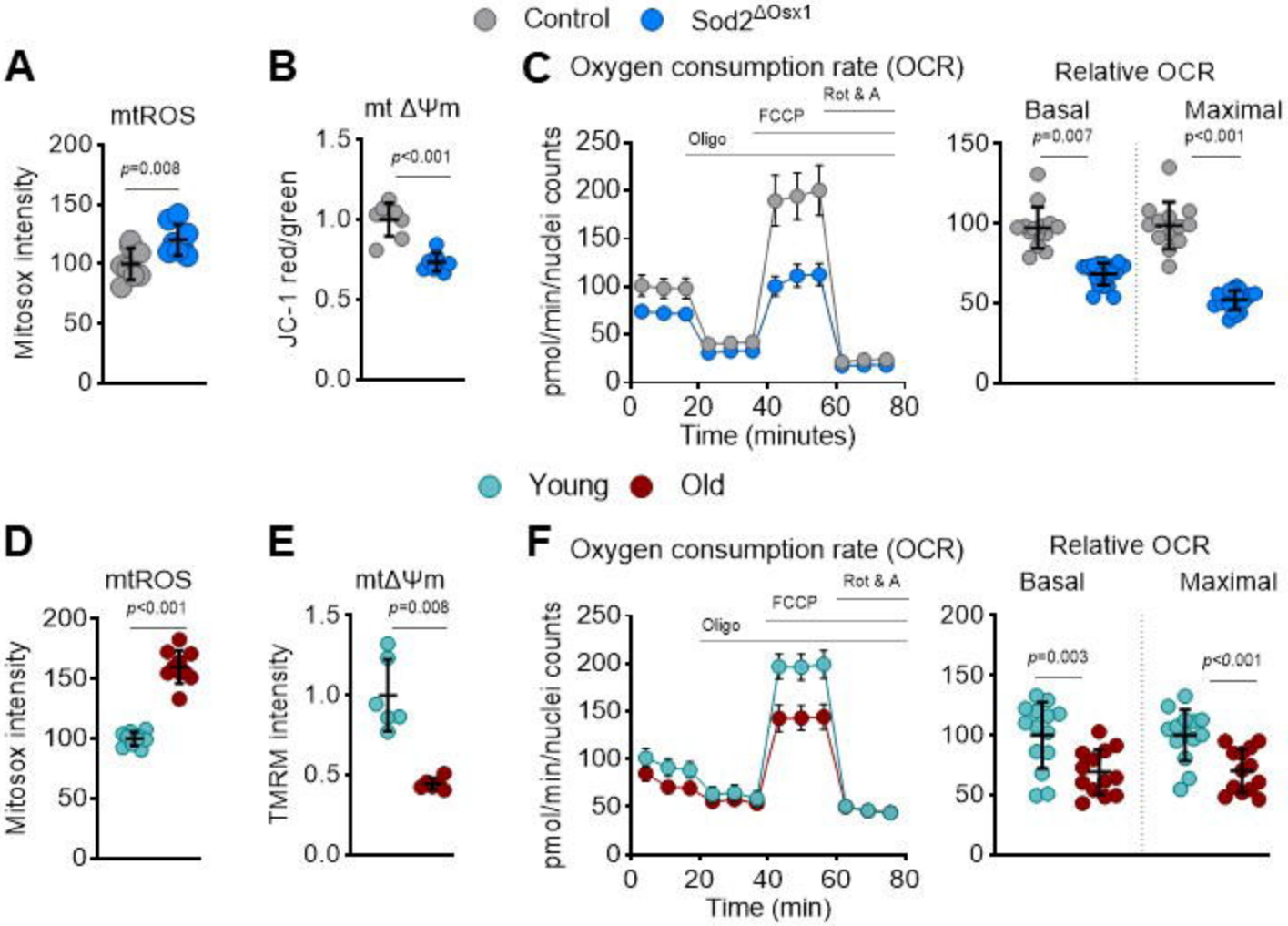

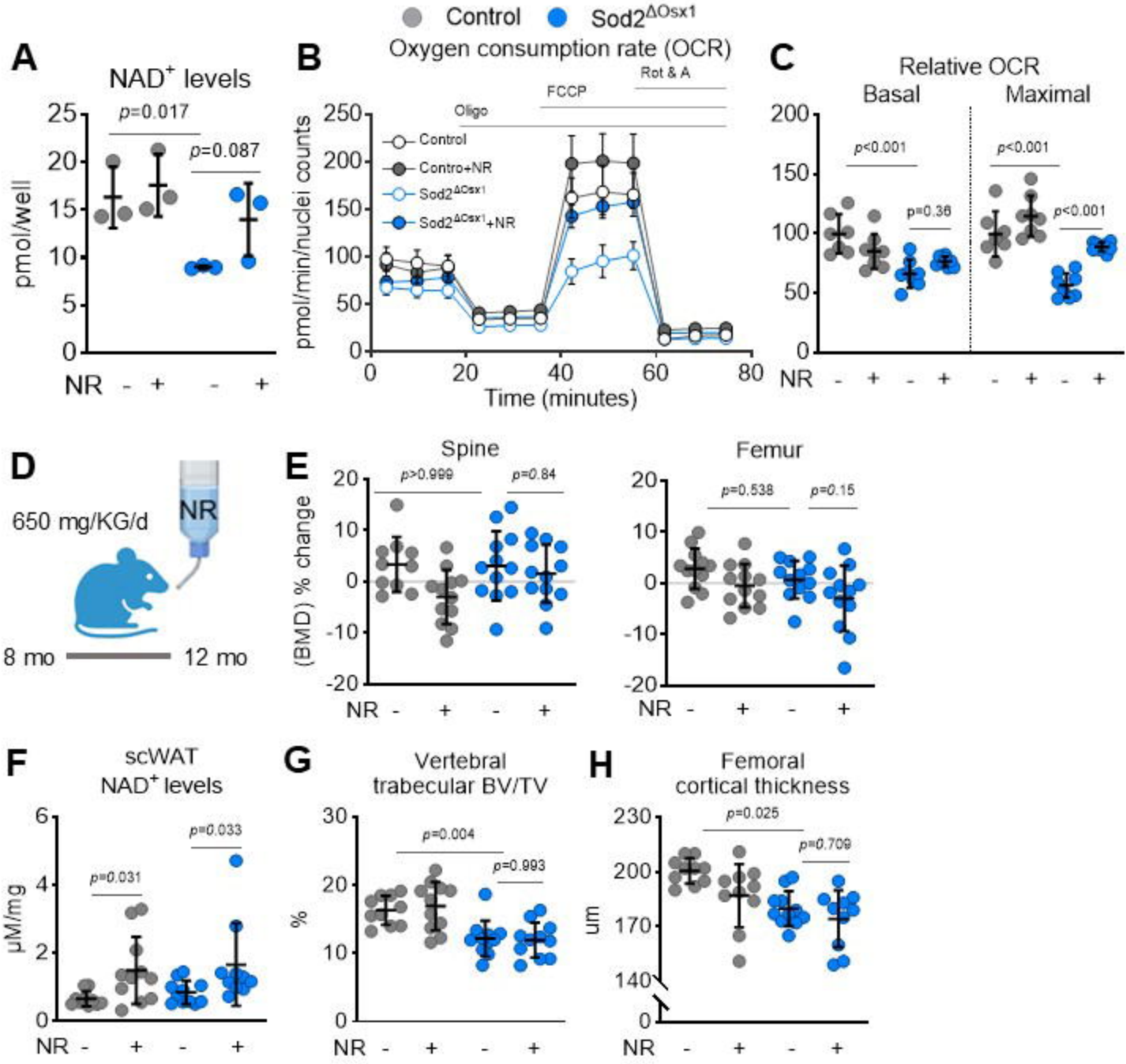

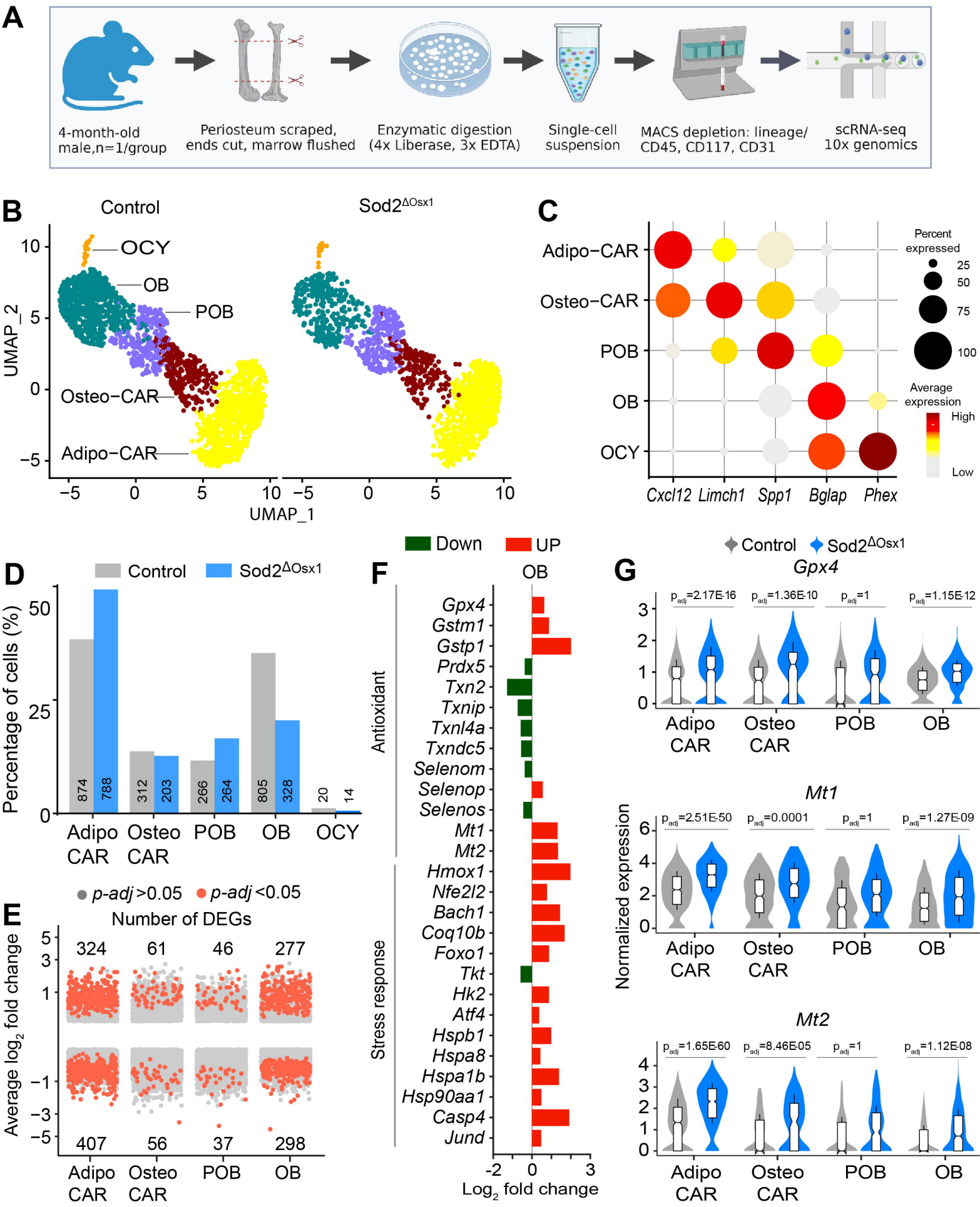
A
4-month-old male,n=1/group
Periosteum scraped, ends cut, marrow flushed
Enzymatic digestion (4x Liberase, 3x EDTA)
Single-cell suspension
MACS depletion: lineage/ CD45, CD117, CD31
scRNA-seq 10x genomics
B
Control
Sod2ΔOsx1
OCY
OB
POB
Osteo−CAR
Adipo−CAR
UMAP_2
UMAP_1
C
Adipo−CAR
Osteo−CAR
POB
OB
OCY
Cxcl12
Limch1
Spp1
Bglap
Phex
Percent expressed
25
50
75
100
Average expression
High
Low
D
Control
Sod2ΔOsx1
Percentage of cells (%)
874
788
312
203
266
264
805
328
20
14
Adipo CAR
Osteo CAR
POB
OB
OCY
E
p-adj >0.05
p-adj <0.05
Number of DEGs
Average log2 fold change
324
61
46
277
407
56
37
298
Adipo CAR
Osteo CAR
POB
OB
F
Down
UP
OB
Antioxidant
Stress response
Gpx4
Gstm1
Gstp1
Prdx5
Txn2
Txnip
Txnl4a
Txndc5
Selenom
Selenop
Selenos
Mt1
Mt2
Hmox1
Nfe2l2
Bach1
Coq10b
Foxo1
Tkt
Hk2
Atf4
Hspb1
Hspa8
Hspa1b
Hsp90aa1
Casp4
Jund
Log2 fold change
G
Control
Sod2ΔOsx1
Gpx4
padj=2.17E-16
padj=1.36E-10
padj=1
padj=1.15E-12
Mt1
padj=2.51E-50
padj=0.0001
padj=1
padj=1.27E-09
Normalized expression
Mt2
padj=1.65E-60
padj=8.46E-05
padj=1
padj=1.12E-08
Adipo CAR
Osteo CAR
POB
OB

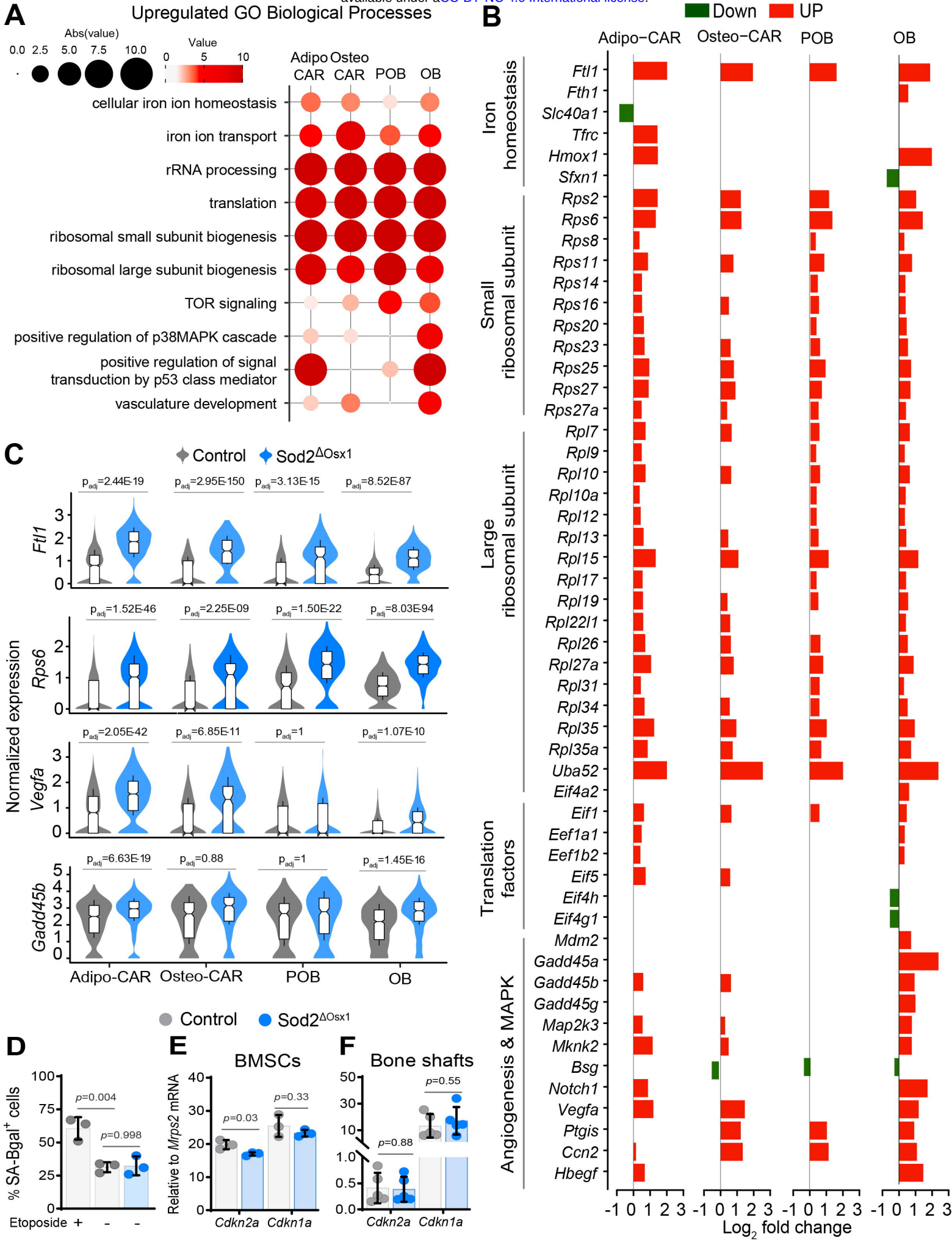

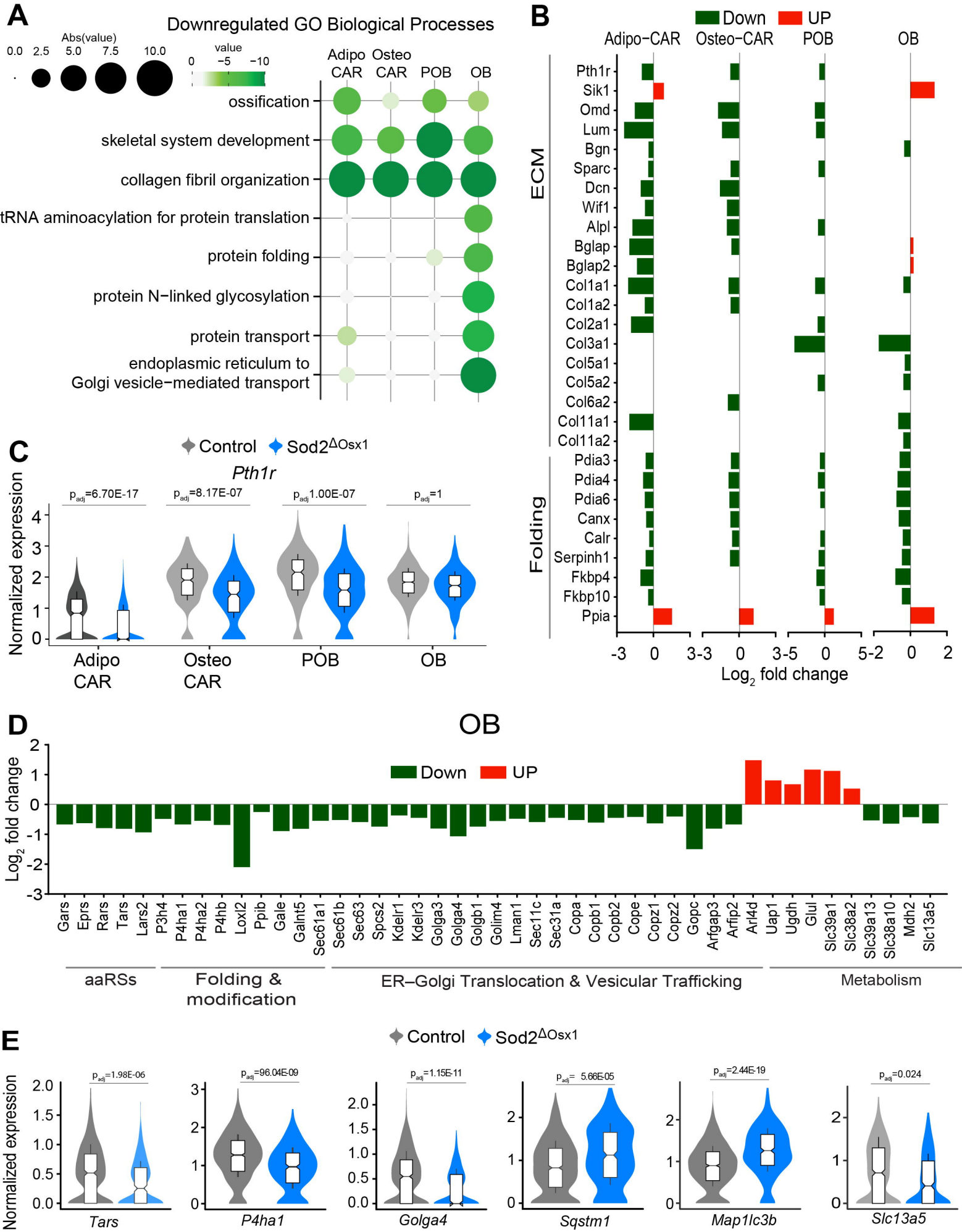
A
Downregulated GO Biological Processes
Abs(value)
0.0 2.5 5.0 7.5 10.0
value
0 −5 −10
Adipo CAR
Osteo CAR
POB
OB
ossification
skeletal system development
collagen fibril organization
tRNA aminoacylation for protein translation
protein folding
protein N−linked glycosylation
protein transport
endoplasmic reticulum to Golgi vesicle−mediated transport
B
Down
UP
Adipo−CAR
Osteo−CAR
POB
OB
ECM
Pth1r
Sik1
Omd
Lum
Bgn
Sparc
Dcn
Wif1
Alpl
Bglap
Bglap2
Col1a1
Col1a2
Col2a1
Col3a1
Col5a1
Col5a2
Col6a2
Col11a1
Col11a2
Folding
Pdia3
Pdia4
Pdia6
Canx
Calr
Serpinh1
Fkbp4
Fkbp10
Ppia
-3 0 3-3 0 3-5 0 5-2 0 2
Log2 fold change
C
Control
Sod2ΔOsx1
Pth1r
padj=6.70E-17
padj=8.17E-07
padj 1.00E-07
padj=1
Normalized expression
Adipo CAR
Osteo CAR
POB
OB
D
OB
Down
UP
Log2 fold change
Gars Eprs Rars Tars Lars2 P3h4 P4ha1 P4ha2 P4hb Loxl2 Ppib Gale Galnt5 Sec61a1 Sec61b Sec63 Spcs2 Kdelr1 Kdelr3 Golga3 Golga4 Golgb1 Golim4 Lman1 Sec11c Sec31a Copa Copb1 Copb2 Cope Copz1 Copz2 Gopc Arfgap3 Arfip2 Arl4d Uap1 Ugdh Glul Slc39a1 Slc38a2 Slc39a13 Slc38a10 Mdh2 Slc13a5
aaRSs
Folding & modification
ER−Golgi Translocation & Vesicular Trafficking
Metabolism
E
Control
Sod2ΔOsx1
Normalized expression
padj=1.98E-06
padj=96.04E-09
padj=1.15E-11
padj= 5.66E-05
padj=2.44E-19
padj=0.024
Tars
P4ha1
Golga4
Sqstm1
Map1lc3b
Slc13a5